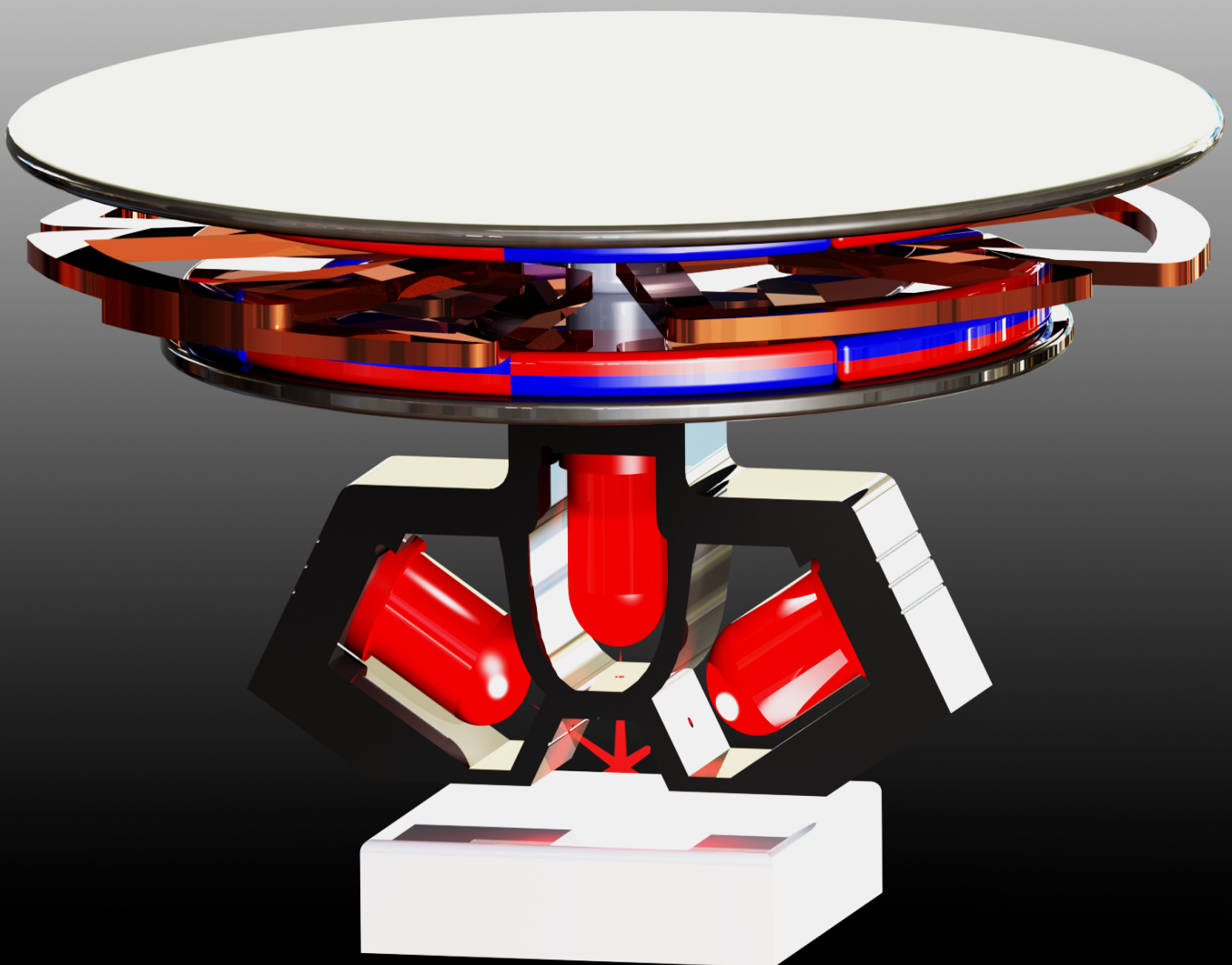


# Department of Precision and Microsystems Engineering

## Design of a three Degrees of Freedom planar precision stage using a single Position Sensitive Detector

Haris Habib

Report no : MSD 2015.031  
Coach : Ir. J.W. Spronck  
Professor : Prof. dr. ir. J. L. Herder  
Specialisation : Mechatronic System Design  
Type of report : Master Thesis  
Date : 5 November 2015





# Design of a three Degrees of Freedom planar precision stage using a single Position Sensitive Detector

by

Haris Habib

to obtain the degree of Master of Science  
at the Delft University of Technology,

to be defended publicly on Thursday November 5, 2015 at 10:00 AM.

Student number: 4009916  
Project duration: September 1, 2014 – November 4, 2015  
Thesis committee: ir. J. W. Spronck, TU Delft, supervisor  
Prof. dr. ir. J. L. Herder TU Delft  
Prof. P. Breedveld TU Delft  
dr. ir. H. HosseinNia TU Delft

An electronic version of this thesis is available at <http://repository.tudelft.nl/>.

Dedicated to my parents

# Abstract

This thesis presents the design and implementation of a precision stage equipped with novel sensing and actuation concepts. This stage is considered among the first stages capable of providing a full rotation as well as planar translations with only one moving part and one sensor. Conventional systems utilize three separate one degrees-of-freedom (DoF) stages for achieving the planar translations ( $x$ ,  $y$ ) and rotation ( $\theta_z$ ). Stacking of individual stages is no longer necessary, which reduces the number of components and complexity and increases the controllability of the system. The stage is intended for use in the field of digital microscopy where it will enable the user to view the sample from all sides without manually relocating the specimen. The underlying mechanical design, sensor technology, electromagnetic modeling and real-time control of such a high-precision planar stage are presented together with the final performance specifications.

One of the components that enable the simplified design is the use of ferrofluid bearings. Ferrofluids contain suspended ferromagnetic particles in a liquid carrier which move to the region of highest magnetic flux. In case of permanent magnets, this occurs on the edges. The ferrofluids around the magnet edges is used to seal a pressurized volume which can carry loads up to 4N in the present design. Figure 2b shows a simplified representation of the ferrofluid bearings. The absence of stick-slip makes this bearing type suitable for high-precision positioning systems.

The mechanical design of the stage is visualized in Figure 1a. The sensor is located below the mover and shielded from stray light. The mover design shown in Figure 1b utilizes the synergy between the magnets required for the ferrofluid bearings and the actuator coils to make the system more compact and lightweight. The double magnet configuration with the coils located in between the magnets ensures that all actuator forces and viscous damping forces from the ferrofluid bearings work through the center-of-mass, hence avoiding unwanted moments. This is necessary since the bearings do not constraint the unwanted tilt motion during acceleration of the mover, which can cause Abbe errors.

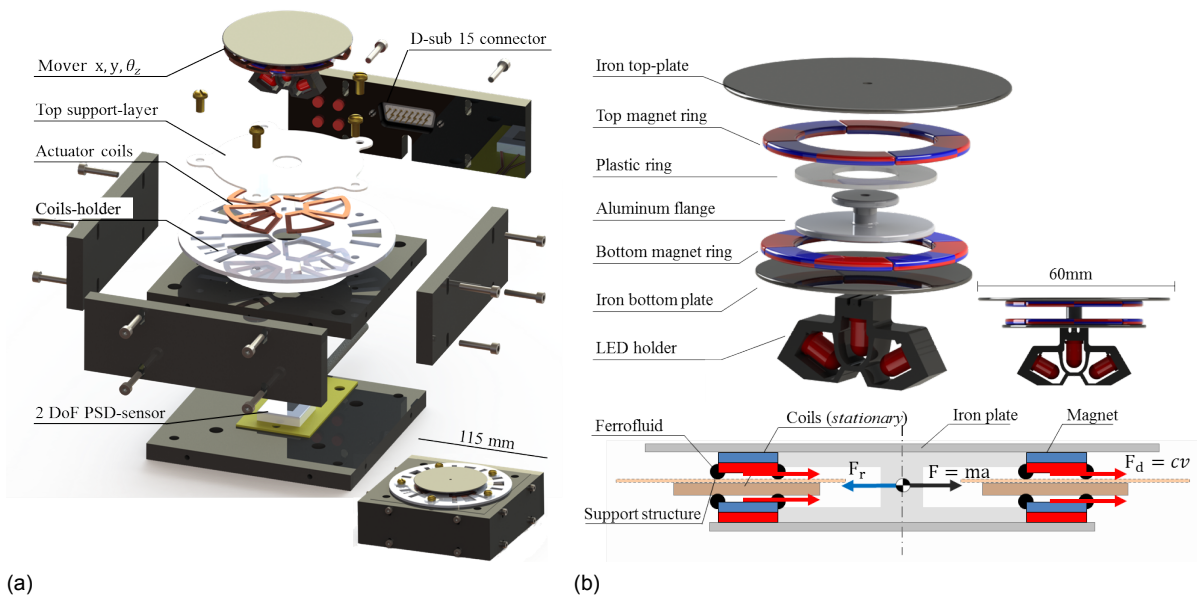


Figure 1: (a) Demonstrator stage including the mover, actuator coils, PSD and laser-cut support structures. (b) Overview of the mover containing iron plates, ring-shaped magnet arrays, an aluminum flange and the LED holder. The vertical location of the center-of-mass  $\odot$  is located in-line with the application point of the resultant actuator forces ( $F_r$ ) and the viscous damping ( $F_d$ ).

The sensing technology applied in the stage includes the use of a 2 degrees-of-freedom (DoF) Position Sensitive Detector (PSD). This affordable sensor produces a signal which is proportional to the location of the centroid of the incident light beam. Instead of measuring the position of one light beam, as the conventional use of this sensor implies, three light beams are sequentially projected on the PSD surface at a frequency of 8.3kHz (visualized in Figure 2a). The modulation frequency is mainly limited by the sensor settling time which is the time required for producing a stable signal once a light source is projected. A sensing algorithm has been developed for sampling and converting these three sensor signals into planar position data:  $x$ ,  $y$  and  $\theta_z$ . The sensor characteristics like non-linearity and position dependent noise are experimentally determined such that they can be accounted for in the control scheme for achieving better positioning accuracies.

The mover is actuated by a novel Lorentz-type actuator configuration, inspired by hard disk actuators. The actuator configuration visualized in Figure 2b, consist of ring-shaped magnet arrays attached to the (moving) top and bottom iron plates. Two coil-sets each containing three coils are attached to the (stationary) frame in between the magnet arrays. When the stage rotates, the magnetic field experienced by the active coil-set weakens and changes polarity. A commutation strategy is developed and successfully implemented in the control scheme to gradually activate the other coil-set. This allows the stage to smoothly rotate around its axis. No commutation is required for planar translations.

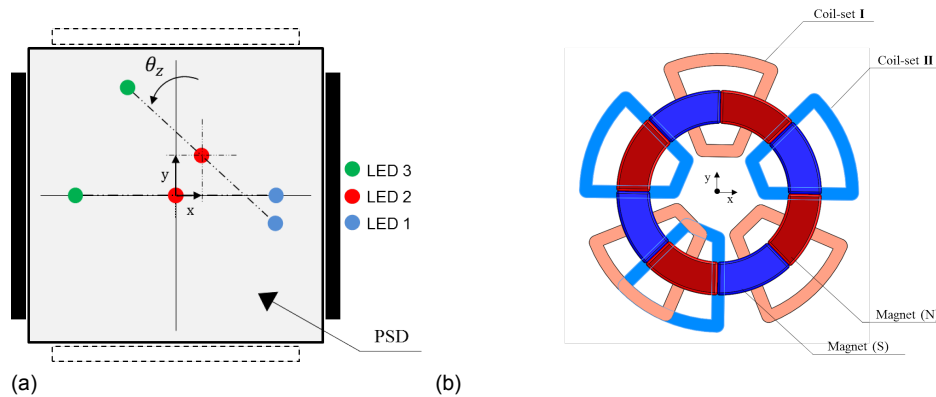


Figure 2: (a) Schematic overview of the PSD measurement configuration. (b) Actuation concept based on the Lorentz actuation principle. Two sets of coils are used to generate forces and a torque in the  $x$ ,  $y$  and  $\theta_z$  direction respectively.

For control purposes the stage is decoupled into three single-input-single-output (SISO) systems. System identification is performed for determining and tuning the controller parameters (PID). A controller bandwidth of 100Hz is achieved in the  $x$ - and  $y$ -direction and 30Hz for the rotational direction. The increasing sensor noise at high frequencies is limiting the system performance. In order to optimize the system, a hybrid controller is proposed. A rapidly traversing stage only needs coarse guidance, it is only near the desired location that high position accuracy is required. The hybrid controller allows the system to switch between a fast controller which allows coarse guidance and a controller with additional filters that can improve the positioning accuracy by a factor two or more.

The present design has a travel range of 9 mm x 9 mm in the  $x$ - and  $y$ -direction and can complete a full rotation around its axis. The ferrofluid bearings can carry loads up to 4N which is eight times more than the required load capacity. Planar steps of 0.1mm and 1mm settle within 0.1s and 0.18s respectively. A rotational step of  $10^\circ$  can be performed within 0.18s. The stage operates with a position accuracy of  $0.2\mu\text{m}$  ( $3\sigma$ ) in the  $x/y$ -direction and  $0.15\text{mrad}$  ( $3\sigma$ ) in the  $\theta_z$ -direction, making the stage applicable for use in the field of precision digital microscopy. In conclusion it can be said that a cost effective and compact precision stage has been developed by using existing sensing and actuating techniques in a new and innovative way.

# Preface

A year ago I started my thesis thinking that it will be a similar experience like the previous years at the university. I couldn't be more wrong! Unlike previous years, the challenges became more individual and where more limited to my own topic rather than tens of people solving the same issues. Luckily I was surrounded with great people who were always there to provide help and guidance or to make things even more complicated.

The first person that deserves my gratitude is my supervisor Jo Spronck. Jo has given me great freedom to wander and think critically. His intellectual guidance was not limited to thesis related topics but also stretched to advice regarding life as an engineer and how every problem can be solved by using ferrofluids. I feel incredibly privileged to have him as my supervisor.

Working in the lab would have been a very lonely experience without Martijn (a.k.a The Don), Floris (a.k.a. Flo Rida), Bart (a.k.a Bartjan) and YangYang. The coffee breaks and vibrant discussions where the highlights of my day, so thank you all.



Picture taking with a thermal camera for determining the hottest guy in the lab. Floris and YangYang are competing for first place.

*Haris Habib  
Delft, October 2015*



# Contents

<b>Abstract</b>	<b>iii</b>
<b>1 Introduction</b>	<b>1</b>
<b>2 Conceptual system design</b>	<b>3</b>
2.1 General requirements	3
2.2 Specifications derived from the general requirements	4
2.2.1 Bandwidth estimation	4
2.2.2 Required actuator forces	4
2.2.3 All motion performed by one moving part	4
2.3 Design considerations	5
<b>3 Mechanical Design</b>	<b>7</b>
3.1 Overall topology and design of the complete stage	7
3.2 Moving stage design	7
3.2.1 Magnet array selection and configuration	8
3.2.2 LED-holder design	9
3.2.3 Application of ferrofluid bearings	9
3.3 Positioning of the actuators	10
3.4 Dynamic deformations	11
<b>4 Sensor Technology</b>	<b>13</b>
4.1 Working principle of a PSD	13
4.2 3 DoF Measurement concept description	14
4.3 Incident light source selection and tuning	15
4.4 Data acquisition and Processing	15
4.4.1 Selecting the light modulation method	16
4.5 Experimental validation of the PSD characteristics	16
4.5.1 Sensor noise sources	16
4.5.2 Determining sensor non-linearity	17
4.5.3 Measurement of sensor noise and the effect of low-pass filtering	18
4.5.4 Drift	19
<b>5 Electromagnetic Design</b>	<b>21</b>
5.1 Actuation concept description	21
5.2 Magnet and coil geometry configuration	22
5.3 Optimizing the actuator force	23
5.3.1 Magnetic circuit design	23
5.3.2 Magnetic field analysis	24
5.3.3 Optimizing the number of windings	26
5.4 Actuator modeling and validation	27
5.4.1 Temperature measurements	27
5.4.2 Motor constant validation	28
5.5 Power amplifiers	29
<b>6 Controller Design</b>	<b>31</b>
6.1 Control system overview	31
6.2 Plant and controller model	31
6.3 Performance specifications	32
6.4 System identification and controller tuning	33
6.4.1 System identification	33
6.4.2 Controller and filter parameter selection	33

6.4.3	Closed loop response . . . . .	35
6.5	Pre-filter design and implementation . . . . .	35
6.6	Integral windup and its effect . . . . .	37
6.7	Commutation between the actuator sets . . . . .	37
6.8	Proposed hybrid control for better position accuracy . . . . .	38
<b>7</b>	<b>Performance measurement</b>	<b>39</b>
7.1	Ferrofluid bearing stiffness measurement . . . . .	39
7.2	Step response . . . . .	39
7.2.1	Step response in the x-direction . . . . .	40
7.2.2	Step response in rotational direction . . . . .	40
7.3	Sensitive for tilt . . . . .	41
7.4	Large angular reference input . . . . .	41
7.5	Repeatability . . . . .	42
7.6	Position stability . . . . .	43
<b>8</b>	<b>Conclusions</b>	<b>45</b>
<b>9</b>	<b>Recommendations</b>	<b>47</b>
<b>A</b>	<b>Review of prior art</b>	<b>49</b>
A.1	Literature summary: Use of a PSD for position measurement and its characteristics . . . . .	49
A.2	Literature summary: Ferrofluids and their applications . . . . .	52
<b>B</b>	<b>Transistor network for LED modulation</b>	<b>55</b>
<b>C</b>	<b>Light intensity at the PSD surface</b>	<b>57</b>
<b>D</b>	<b>Identification of the PSD characteristics</b>	<b>59</b>
<b>E</b>	<b>Alternative actuator concept</b>	<b>61</b>
<b>F</b>	<b>Theta controller design</b>	<b>63</b>
<b>G</b>	<b>Transformation matrices</b>	<b>65</b>
	<b>Bibliography</b>	<b>67</b>

## Introduction

Precision stages are widely used in the field of digital microscopy or other types of scientific and industrial applications. The introduction of motorized stages has dramatically improved the range of operation. Planar stages allow the user to make fine repetitive position adjustments. In the field of biomedical studies for example it is common practice to capture multiple images of a single sample with overlapping field of view. These images are then combined (“stitched”) into a larger high resolution image [18]. With image stitching, the amount of information captured increases with the number of images taken.

By placing the digital microscope at an angle and rotating the stage, it becomes possible to view the sample from all sides without manually relocating the specimen. This capability is visualized in Figure 1.1. Conventional system achieves a similar motion by stacking a X/Y-stage on top of a rotational stage. This results in a system with multiple moving masses with increased (control) complexity and cost.

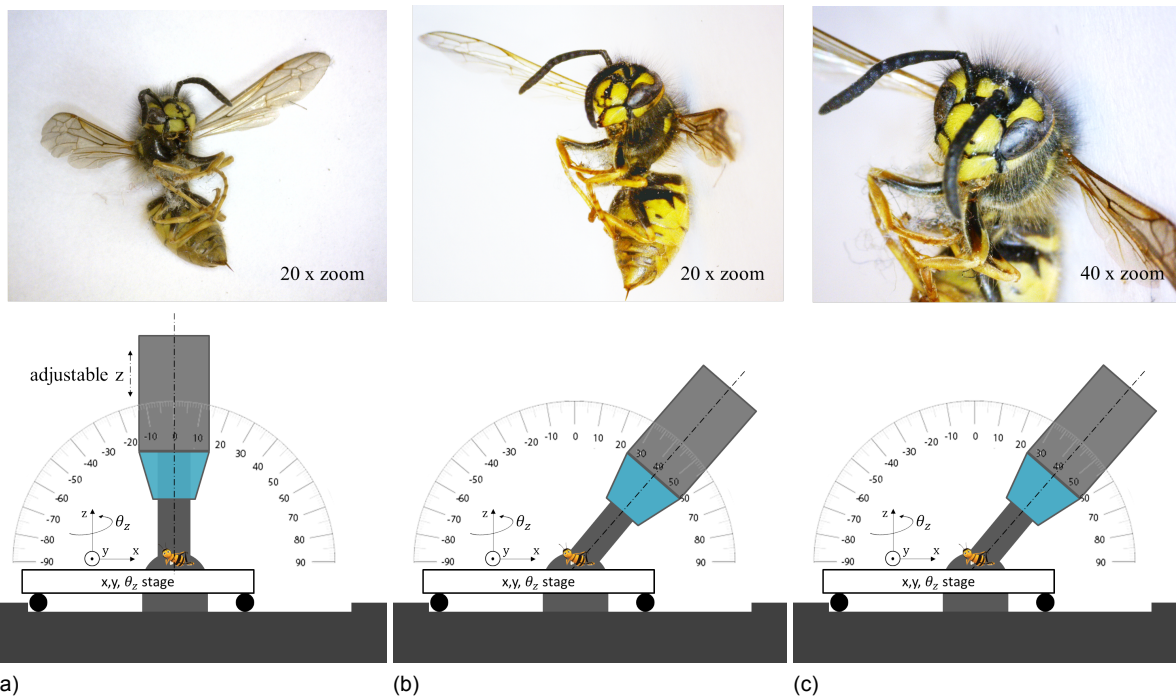


Figure 1.1: (a) Sample observed from different angles (top-view (a) and side-view (b)(c)). A rotating stage allows the sample to be viewed from all sides without manually relocating the microscope or specimen.

## Thesis objective

This thesis presents the design of a low cost precision stage capable of performing large translations and rotation with one movable part. In addition only one sensor, a Position Sensitive Detector (PSD), is used to measure all planar degrees-of-freedom (DoF). The PSD is an optical sensor that can measure the position of a light beam on the sensor surface, which is a uniform resistive layer on the surface of a semiconductor substrate. In [12] and [17] it is proven that the position of multiple light beams, sequentially modulated at the PSD surface, can be retrieved. Based on this principle, Xiangyun He developed a three DoF measurement system in her master thesis [5].

A major part of this thesis focuses on developing and tuning a sensing algorithm that can sample position signals from multiple incident light beam on the PSD surface and translate these into planar position data:  $x$ ,  $y$  and  $\theta_z$ . The light modulation technique will be optimized for achieving a high signal-to-noise ratio.

The second area of focus is the development of a planar actuation concept that allows the stage to translate in a desired planar direction as well as perform rotations around its axis. Integrating the actuation concept with the proposed sensing concept will result in a versatile stage, usable in the field of digital microscopy.

**The objective of this thesis can be formulated as:** Design of a low-cost and compact planar precision stage capable of making large translations and rotate around its axis by implementing the proposed sensing concept using one PSD.

## Thesis overview

The first step in arriving at a concept design for a mechatronic system is to gain insight in the requirements. These are deduced in Chapter 2 with the application of digital microscopy in mind. The project is multi-disciplinary, each having its own challenges. The mechanical design of the stage will be discussed in Chapter 3. Research on the sensing algorithm and performance of the PSD is performed in Chapter 4. The actuators are designed, modeled and discussed in Chapter 5. In Chapter 6 the Controller Design is discussed. The performance of the complete system is presented in Chapter 7. Finally in Chapter 8 the conclusions and in Chapter 9 the recommendations are listed.

Not all the detailed work is documented in one of the chapters. Multiple appendices are included for example regarding prior art literature, the electric design of components or other topics.

## Contributions of the thesis

The technical realization of the worlds first planar positioning stage using a single PSD to measure all planar DoF is the main contribution of this work. The large stroke in the  $x$ - and  $y$ -direction and the ability to rotate  $360^\circ$  with only one moving part is something unique. Specific contributions are the design, analysis and control of such a stage. The mechanical design allows a compact precision precision stage to be built with use of low-cost components. The electromagnetic design enables the stage to compete with current stages on the market in terms of accelerations. A large rotational stroke is realized by means of commutation between actuator coils. The synergy between the actuator magnets and the ferrofluid bearing is successfully implemented and validated resulting in a high bearing stiffness without stick-slip behavior and static friction.

# 2

## Conceptual system design

### 2.1. General requirements

With the possible application of digital microscopy in mind, a list of general requirements is created and summarized in Table 2.1. The total translational range of the stage is set to be 10 mm x 10 mm, which is enough for most biomedical applications like tissue analysis. Increasing the range is possible by simply replacing the PSD with a larger PSD and up-scaling some components without major design adjustments. The rotational range is set to be at least 360°, allowing the sample to be viewed from all sides once placed on the stage. Furthermore, the stage should be capable of competing with current stages on the market in terms of positioning accuracy and time required to perform a step motion. A short settling time allows more images to be taken within a time period.

The position accuracy of conventional planar stages ranges from sub-nanometers up to several micrometers, whereby short stroke stages tend to have higher position accuracies. Also the system cost increases with increasing position accuracy and can reach thousands of euros [21]. For most applications sub-micrometer positioning accuracy is more than enough, like in the field of blood cell research for example where the size of a human blood cell is  $\pm 8\mu\text{m}$ .

The positioning accuracy in the rotational direction is set to be  $< 0.01^\circ$ . This accuracy value is derived from the performance specifications of existing rotation stages [4], since nothing comparable with proposed  $XY\theta_z$ -stage exists on the market. With the application in mind, the load capacity is derived to be above 50 grams.

Table 2.1: General system requirements

Requirement	Planar translation
Range, translation x-y	$\geq 10\text{mm} \times 10\text{mm}$
Positioning accuracy in x and y	$\leq 1\mu\text{m} (3 \cdot \sigma)$
Range, rotation	$\geq 360$
Positioning accuracy in $\theta_z$	$< 0.01^\circ$
Settling time for 20° rotational step	$\leq 1 \text{ s}$
Settling time for 0.1mm planar step	$\leq 0.1 \text{ s}$
Load capacity	$\geq 50 \text{ grams}$

## 2.2. Specifications derived from the general requirements

### 2.2.1. Bandwidth estimation

Floor vibrations are the main external disturbance sources to be accounted for. The virtual connection between the moving stage and the reference frame (fixed to the floor) should be stiff enough to suppress these floor vibrations. From the work performed by Max Cafe [2] and others graduates in the department, the maximum derived floor vibration accelerations ( $a_{vib}$ ) range from  $2.2 \frac{mm}{s^2}$  until  $37 \frac{mm}{s^2}$ . The highest acceleration value is chosen, such that the stage performs well in the worst case scenario. Thus the required control force can be described as:

$$F_{control} = k\varepsilon = ma_{vib} \quad (2.1)$$

where  $\varepsilon$  is the maximum positioning error, which is limited to  $1\mu m$  and  $m$  is total moving mass. The required minimum control bandwidth of 30Hz is calculated using the equation below:

$$f_{bw} = \frac{1}{2\pi} \sqrt{\frac{a_{vib}}{\varepsilon}} \quad (2.2)$$

### 2.2.2. Required actuator forces

There are basically two different actuation modes that can be distinguished. The stage will mostly require small forces to counteract the ground vibrations. The required disturbance rejection force can be calculated using:

$$F_{dist} = ma_{vib} \quad (2.3)$$

where the total moving mass  $m = 65g$ . This results in a  $F_{dist}$  of 0.002N

The stage should also be able to perform a step of  $100\mu m$  within 0.1 sec. Simon van Veen derived the following equation in his master thesis [22] for calculating the required force for a mass damper system performing a step function:

$$F_{step} = \frac{c^2 x_s}{m(e^{-\frac{ct_s}{m}} - 2e^{\frac{c(\tau-t_s)}{m}} + \frac{c}{m}(2\tau - t_s) + 1)} = 0.02N \quad (2.4)$$

The equation takes into account that damping works against the acceleration force while it helps during the deceleration when the desired position is almost reached. In the equation above,  $c$  is the damping coefficient,  $x_s$  is the step size and  $t_s$  the step time and  $\tau$  represent a time offset. The main unknown in this equation is the damping  $c$ , which depends on velocity, temperature, bearing geometry, magnet strength, ferrofluid type and volume and other variables. A safety factor of 10 is applied due to the high level of uncertainty in the application of the novel bearing type which is presented in paragraph 3.2.3. An overestimated safety factor will benefit the step response since more force will be available for accelerating the mover rather than overcoming friction. The required actuator force is thus:

$$F = F_{dist} + 10 \cdot F_{step} \approx 0.2N \quad (2.5)$$

### 2.2.3. All motion performed by one moving part

Based on the requirements the stage should be able to complete at least one full rotation around its axis. This can be achieved by stacking a X/Y-stage on top of a rotational stage, but would result in a system with multiple moving masses with increased (control) complexity and cost. The goal is to achieve the same motion capabilities with only one moving mass. Planar Lorentz actuators are designed that allow translations and a full rotation by means of commutation between the coil-sets. This concept is explained in Chapter 5.

## 2.3. Design considerations

The following design considerations are taken into account during the design, manufacturing and validation phase:

### **Cost and complexity**

The stage is designed to be compact and affordable, making it useful for a broad market range. The components used should be cost effective and simple to produce, possibly allowing mass production in the future.

### **Adjustability**

Since almost all components will be produced in-house, the stage is prone to misalignment due to production tolerances. The design should therefore allow manual adjustment of parts once assembled.

### **Repeatability**

The performance results obtained in this work should be reproducible elsewhere using the same setup and design suggestions.



# 3

## Mechanical Design

### 3.1. Overall topology and design of the complete stage

The complete system including all components is shown in Figure 3.1. The main components are the moving stage which will be discussed in the next section together with the actuator coils and PSD (Chapter 4). Six Lorentz actuator coils are implemented at the base, while the magnets are attached to the mover. In Chapter 5 the parameters concerning shape, size and power output of the actuators are discussed. Ferrofluid is applied to the same magnets to carry the mover. Finally the PSD, on which multiple light beams are sequentially modulated, is mounted below the moving stage and shielded from stray light.

### 3.2. Moving stage design

The mover visualized in Figure 3.2 will be used to carry microscopic samples or other lightweight objects. These samples could require shielding from the magnetic field and from heat generated in the actuator coils. For that reason an iron plate is used as top-plate. Next, a ring-shaped magnet array, containing ferrofluid, is attached to the top plate. An aluminum flange is used to separate the bottom magnet array from the top. The main reason for designing this double structure is that the magnetic field strength increases with 81% while the mass will increase by only 56.1% (as calculated in section 5.3), thus allowing higher accelerations. At the bottom of the moving stage a LED-holder containing 3 LEDs is attached to the second metal plate.

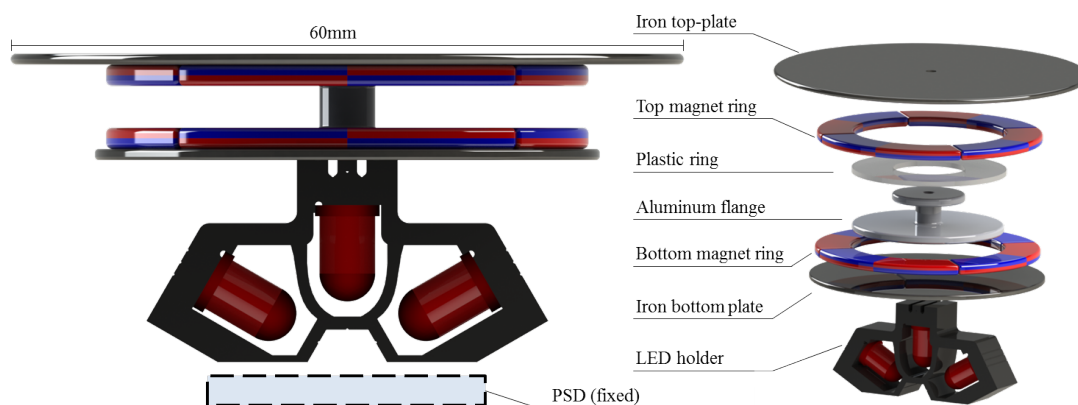


Figure 3.2: Complete overview of the mover containing two metal plates, two ring-shaped magnet arrays, an aluminum flange and a LED holder containing three LEDs.

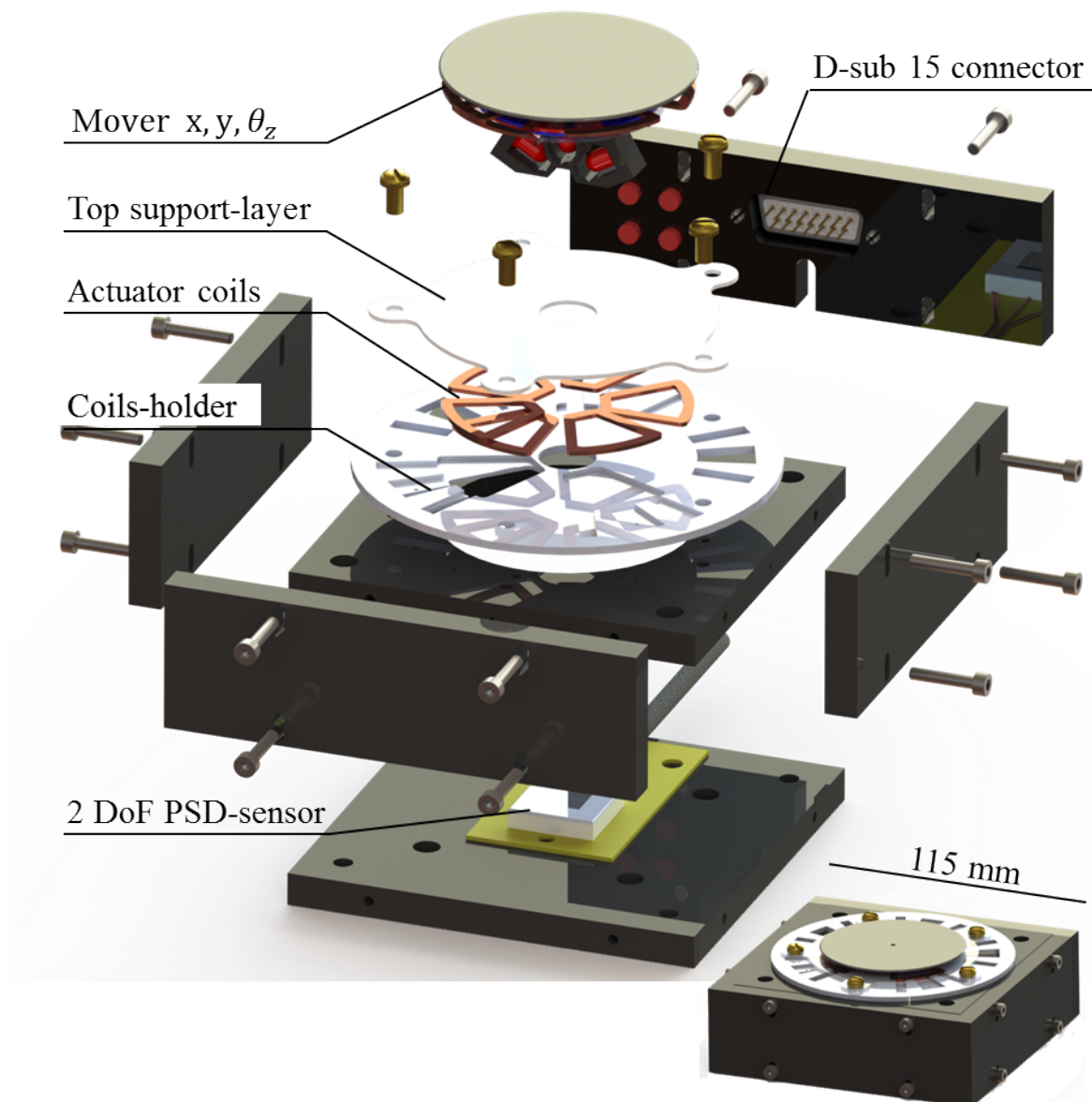


Figure 3.1: Visualization of the demonstrator stage showing the mover, actuator coils, PSD and laser-cut (support) structures.

### 3.2.1. Magnet array selection and configuration

The ring-shaped magnet array is one of the most crucial parts of the stage. Careful attention has been paid to the magnet selection process, which includes finding a magnet with the right dimension and strength. Figure 3.3a shows one magnet including the most important dimensions which include. A larger magnet width will enable a longer coil length to be located inside the magnetic field. The angle  $A_m^\circ$  should be at least  $120^\circ$ . Otherwise commutation based on the applied principle (explained in section 6.7) will not be applicable. Figure 3.3b shows the complete ring-shaped magnet array. It proved to be challenging to find the magnet with the right dimensions. Even some of the largest magnet specialists did not have something in stock, and a single custom order would have cost hundreds of euros. For that reason, the magnets from several old hard-disks are used. In the future, a large batch can be ordered, resulting in lower costs per piece.

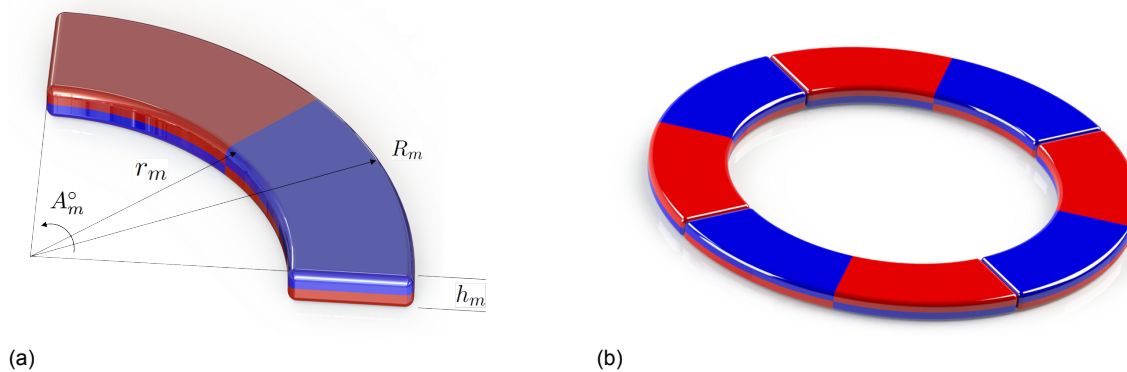


Figure 3.3: (a) One magnet segment including the dimension:  $R_m = 21.5\text{mm}$ ,  $r_m = 14.5\text{mm}$ ,  $A_m^\circ = 90^\circ$ ,  $h_m = 1.9\text{mm}$ . (b) Complete magnet array consisting of four magnets.

### 3.2.2. LED-holder design

The LED holder is laser-cut out of PMMA. The laser-cutting process gives the design freedom to create complex structures while maintaining tolerances that are low enough, making it suitable for manufacturing the LED-holder and other parts. The holder in Figure 3.4 is designed to hold 3 LEDs, each having their own pin-hole. This ensures that maximum LED power can be transmitted to the PSD surface, as described in section 4.3. The LED-holder also serves as a base where the LED-wires are wound around. The wires are inserted from four different sides to minimize the added stiffness onto the moving stage.

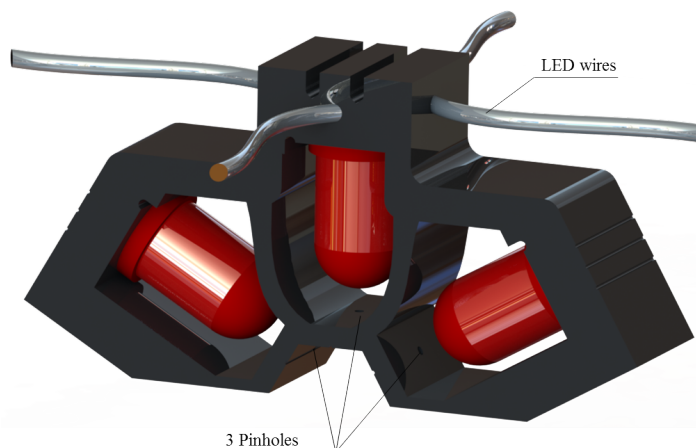


Figure 3.4: 3D visualization of the laser-cut LED-holder containing three LEDs. Light is transmitted to the PSD surface through individual pinholes at the bottom of the holder.

### 3.2.3. Application of ferrofluid bearings

Ferrofluid bearings are proven to be applicable in precision stages, for example in [2], [22] and [8]. Ferrofluids consist of a carrier fluid, nanoscale ferromagnetic particles and a coating on each particle which prevents agglomeration (Figure 3.5a), even when a strong magnetic field is applied. Ferrofluids tend to move to the region with the highest magnetic flux. For permanent magnets the highest flux is found around the edges. Thus when ferrofluid is applied on a permanent magnet, it clusters around the edges, thus building up a pressure ( $p_s$ ). Figure 3.5b shows how this looks for a single magnet, while in Figure 3.5c ferrofluid is applied to the complete magnet array. This provides the basis of a (translational) ferrofluid bearing using permanent magnets. More information regarding ferrofluids and their applications can be found in for example [6] and [14].

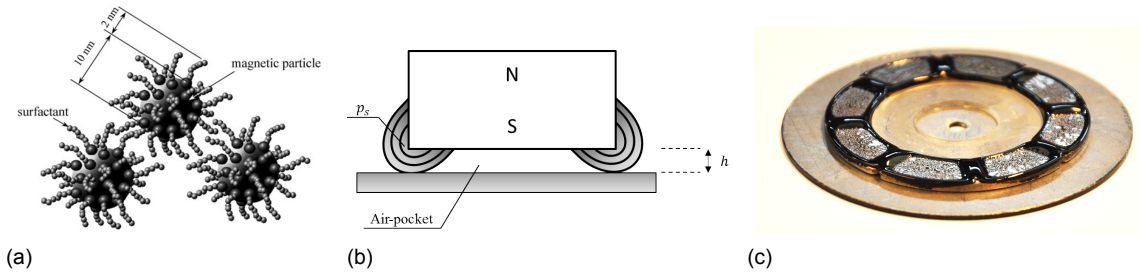


Figure 3.5: (a) Schematic view of the coated magnetic ferrofluid particles [14]. (b) Schematic representation of the pressure built-up in a ferrofluid volume around the magnet edge. (c) Ring-shaped magnet array containing ferrofluid. In total there are 8 air-pockets that are sealed by ferrofluid.

Translational ferrofluid bearings can be divided into two main categories: the first one being bearings that only use the flotation effect and secondly bearings that employ the ferrofluid as a seal for a pressurized volume which bears the load [10]. Both categories utilize the great advantage of ferrofluid bearings, namely that there is no direct contact between the moving parts. This results in almost no static friction and stick-slip. However, the viscous friction can be large depending on the fluid viscosity. For our purpose we use ferrofluid (type APG S12n) with a synthetic oil as carrier fluid and magnetite particles ( $Fe_3O_3$ ).

The translational bearing used in the moving stage is visualized in Figure 3.6. It uses the ferrofluid pressure seal to support load in the upward and downward direction. In [22] it was computed and measured that the pressure inside the air-pocket can be raised up to 50mbar. Applying the same principles would result in a load capacity of almost 4N for the magnet configuration used. A vertical stiffness of  $8 \frac{kN}{m}$  is achieved with one magnet comparable of size with the magnets used in this work. Thus for the 8 air pockets, the predicted stiffness is  $64 \frac{kN}{m}$ . The stiffness could even be higher due to the pretension that is caused by the ferrofluid at the bottom magnet ring.

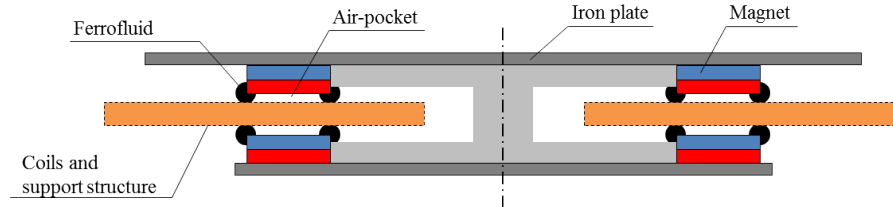


Figure 3.6: Schematic visualization of the translational ferrofluid bearing applied on the moving stage. The ferrofluid is employed as a seal to create an air pocket which bears the load.

### 3.3. Positioning of the actuators

Planar Lorentz actuators are used to actuate the stage in the  $x$ ,  $y$  and  $\theta_z$  direction. To avoid unwanted movement in the uncontrolled directions the point of actuation should be chosen such that the resultant moment around the  $x$ - and  $y$ -axis remains zero, giving  $\sum M_{x,y} = 0$ . In Figure 3.7 the center of mass is indicated as  $\bullet$ . The damping force  $F_d$  caused by the ferrofluid bearings acts symmetrically around the same horizontal line at which the center of mass lies and where the actuator force is acting.

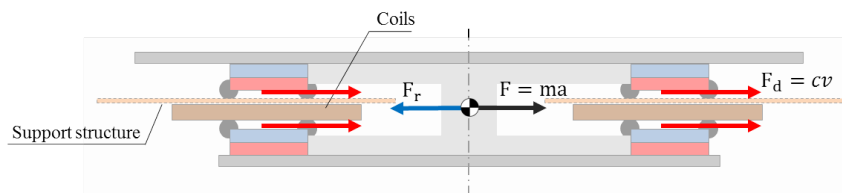


Figure 3.7: The vertical location of the center-of-mass is located in-line with the actuator force and the viscous damping force from the bearings. No unwanted moments are created which could cause the mover to tilt.

### 3.4. Dynamic deformations

A modal analysis is performed to determine the internal eigenfrequency of the mover. The eigenfrequencies must be sufficiently higher than the required control bandwidth to avoid vibrations. These vibrations can induce measurement errors and make the controllability of the stage more challenging. To check if the mover is stiff enough a COMSOL simulation has been performed to get an impression of the first eigenmodes and the frequencies they appear at. Before running the simulation certain assumptions were made:

- The ferrofluid is modeled as a boundary layer with the expected ferrofluid bearing stiffness calculated in section 3.2.3.
- The mass of the magnets is added to the mass of the metal plates as additional weight. This will result in a lower and probably more realistic eigenfrequency ( $f = \sqrt{\frac{k}{m}}$ ).
- The components (top-plate → aluminum flange → bottom-plate → LED-holder) are glued together. The glue is modeled as a thin elastic layer, which significantly reduces computational cost and time without sacrificing the accuracy of the simulation.

Figure 3.8 shows the first two eigenmodes which can be described as flapping modes around the glued connection points. At a frequency of 234Hz the first natural frequency is well above the required bandwidth frequency. It will thus not cause any control difficulties.

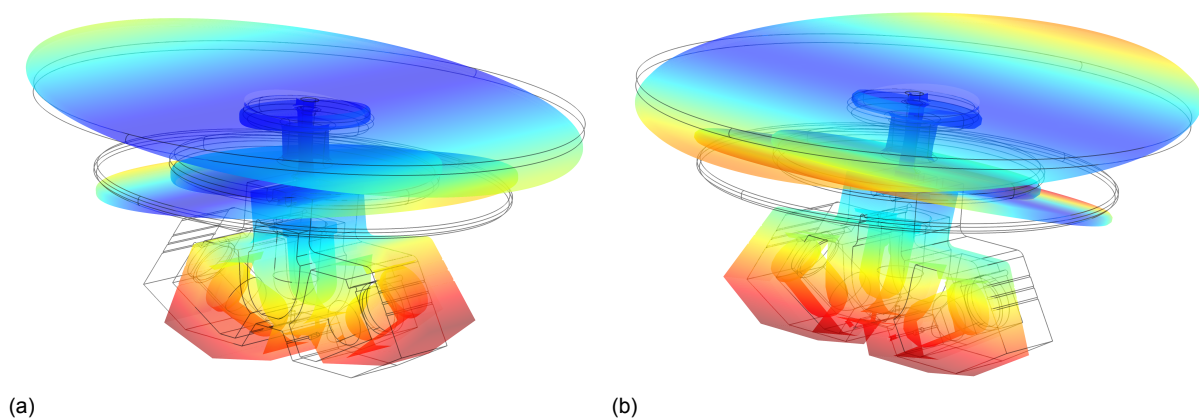


Figure 3.8: (a) COMSOL simulation of the first eigenmode at a frequency of 234Hz (a) and the second eigenmode at a frequency of 240Hz (b). The motions are mainly caused by the glue in between the sub-components.



## Sensor Technology

### 4.1. Working principle of a PSD

The Position Sensitive Detector (PSD) consists of a uniform resistive layer on both surfaces of a semiconductor substrate. When a light beam is projected, a photopotential is produced proportional to the location of the centroid of the light spot. The position signal is extracted via pairs of electrodes on the ends of the resistive layers. This phenomenon is called the lateral photoeffect (LPE) [17]. This effect was first observed by Schottky in 1930 [19] but it would be Wallmark who used this effect to measure the position of a spot of light [23]. Figure 4.1a shows the schematic representation of a 2 DoF PSD including the pairs of electrodes. On a two-dimensional PSD, the location of the light spot is given by:

$$x = \frac{V_{x1} + V_{x2}}{V_{x1} - V_{x2}} \cdot \frac{L}{2} \quad (4.1)$$

$$y = \frac{V_{y1} + V_{y2}}{V_{y1} - V_{y2}} \cdot \frac{L}{2} \quad (4.2)$$

where  $L$  is the distance between two opposing electrodes and  $V_{x1}$ ,  $V_{x2}$ ,  $V_{y1}$ ,  $V_{y2}$  are the voltages which are first extracted as currents by the electrodes and then amplified and converted into voltages.

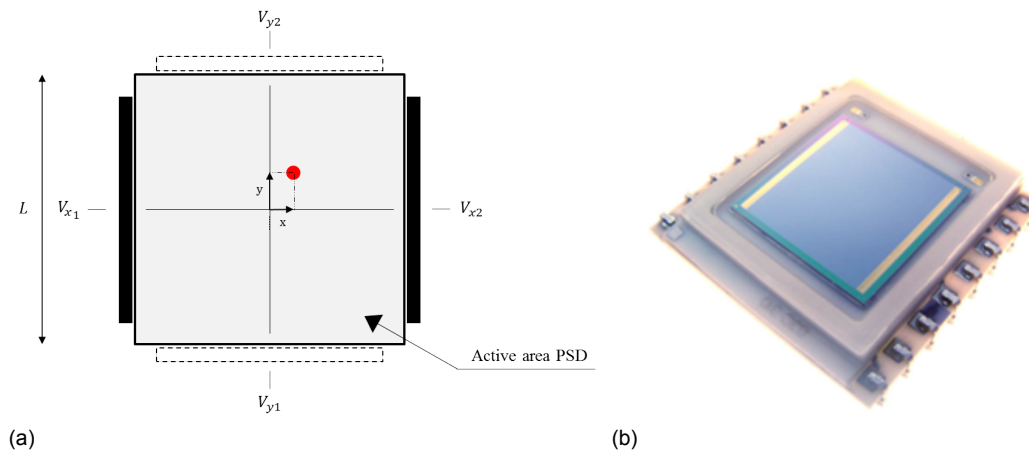


Figure 4.1: (a) Schematic representation of the PSD including pair of electrodes. (b) A duolateral two-dimensional PSD used in the final design, model: SiTek 2L10\_SU65\_SPC01.

The main area of application of PSDs is for example precision optical alignment, biomedical applications, robotics and position information systems. PSDs based on the LPE can provide continuous position information over large areas with no internal discontinuities. This is their major advantage over arrayed discrete devices such as charge coupled devices and photodiodes. The sensor is insensitive to external magnetic fields, making it very useful for implementation in a mechatronic system involving electromagnetic actuators [24].

## PSD selection

PSDs are manufactured in several sizes. The most reputable manufacturers are Hamamatsu, UDT Sensors Inc., and Sitek. Hamamatsu provides cheap sensors which have become better in the last years. Still, Sitek is known for producing PSDs with the highest accuracy and linearity, which is why a SiTek PSD (shown in Figure 4.1b) is selected.

## 4.2. 3 DoF Measurement concept description

A single PSD is used to measure the displacements in all three planar DoF. By sequentially modulating three light beams on the sensor surface, three position signals equivalent to the position of the light beams is retrieved. The idea of modulating multiple light beams on a PSD is already demonstrated by [17] and [12]. A sensing algorithm has been developed for sampling and translating these sensor signals into planar position data:  $x$ ,  $y$  and  $\theta_z$ , visualized in Figure 4.2.

The three LEDs are mounted on the moving stage while the PSD is locked in position. The position of the stage in the  $x$  and  $y$  direction can be detected by the relative movement between LED 2 and the PSD. In Figure 4.2 the angular rotation  $\theta_z$  is calculated using the position coordinates of the three LEDs, according to equation 4.3:

$$\theta_z = \arctan\left(\frac{y_2 - y_{1,3}}{x_2 - x_{1,3}}\right) \quad (4.3)$$

where  $y_{1,3}$  and  $x_{1,3}$  mean that either the information from LED1 or LED3 will be used. This way the full active area of the sensor can be used. If the stage moves in the  $+x$  direction, LED 1 will get out of range. This means that only position information from LED 2 and LED 3 can be used for calculating  $\theta_z$ . Only information from LED 1 and LED 2 can be used in case the stage moves too far in the  $-x$  direction. The angle  $\theta_z$  can also be calculated using equation 4.4 or 4.5.

$$\theta_z = \arcsin\left(\frac{y_2 - y_{1,3}}{d}\right) \quad (4.4)$$

$$\theta_z = \arccos\left(\frac{x_2 - x_{1,3}}{d}\right) \quad (4.5)$$

where  $d$  is the distance between the LED in the middle and the outside LEDs. As  $d$  increases, the error in the angular position measurement decreases.

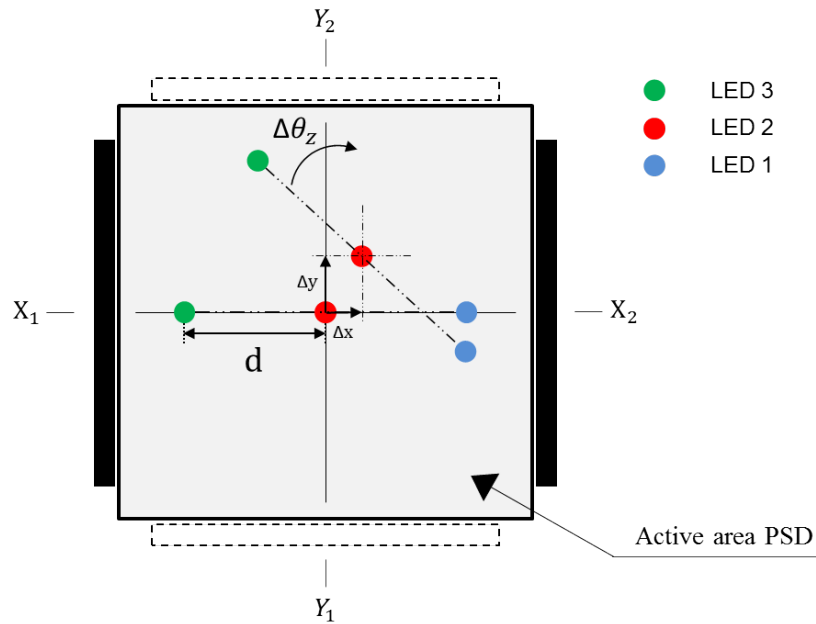


Figure 4.2: Schematic overview of the PSD measurement configuration including 3 LEDs at a distance  $d$  from each other.

### 4.3. Incident light source selection and tuning

When thinking of a light source used for measuring displacements, one might think of using a laser instead of a LED. One of the advantages of a laser is that the light that comes out is (almost) non-divergent. This enables precise calculation of the position of the light spot. The high optical power enables us to use a small diameter for the pinhole while having sufficient light power at the PSD surface. The performance of both light sources is measured in combination with the PSD. Already in an early testing stage, it could be concluded that the laser was not suitable for the design due to the heat generation, thus further investigation is performed on the performance of a LED. The advantages of the LED, like being lightweight, cheap and having a low heat output make it perfectly suitable for our design.

A test setup is built consisting of a LED with variable pinhole diameters through which a light beam is projected on the PSD. In Appendix C, it is shown that the noise errors coming from the PSD is Gaussian distributed. Therefore the  $3\sigma$  noise value is taken as a performance value. From the test results in Figure 4.3a there seems to be an optimal light intensity resulting in minimum noise. This value can be reached with different pinhole diameters and LED power outputs, but a larger diameter decreases the active working area of the PSD as visualized in Figure 4.3b. Therefore, a pinhole diameter of 0.4mm is chosen.

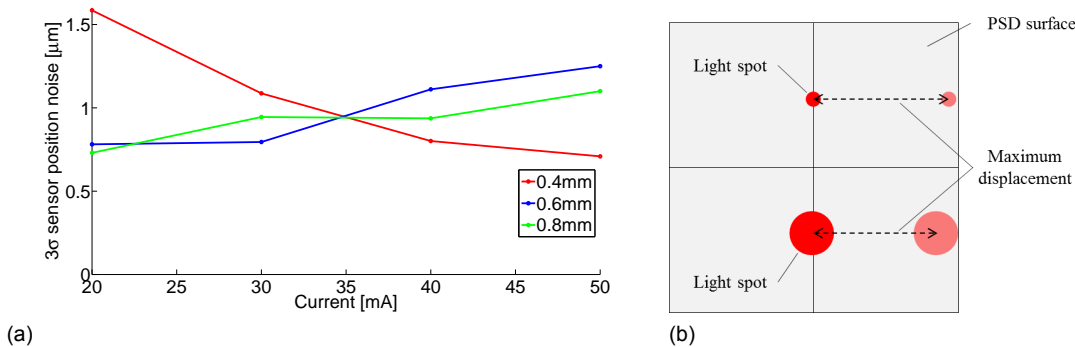


Figure 4.3: (a) Sensor noise proportional to the light intensity at the PSD surface. The maximum allowed current through the LED is 50mA. (b) Two differently sized light spots on a PSD surface. A larger light spot decreases the maximum displacement that can be measured.

### 4.4. Data acquisition and Processing

The PSD outputs four small currents generated from the light emitted on the surface of the PSD, while the acquisition of the A/D converter is in voltages. An amplifier with a large amplification factor is placed between the PSD and the A/D converter as visualized in Figure 4.4. The amplifier is located closely to the PSD to minimize the effect of noise on the low current signal from the PSD. The voltage from the amplifier circuit goes directly into a 16 bit A/D converter, sampling at 25 kHz. The maximum theoretical resolution of a 16 bit A/D converter is 15nm over a range of 10mm. The A/D converter is bipolar, meaning that it will convert positive and negative voltages, and has a range of  $\pm 10\text{V}$ . Once the analog signal is converted into digital data, it is further processed for position detection.

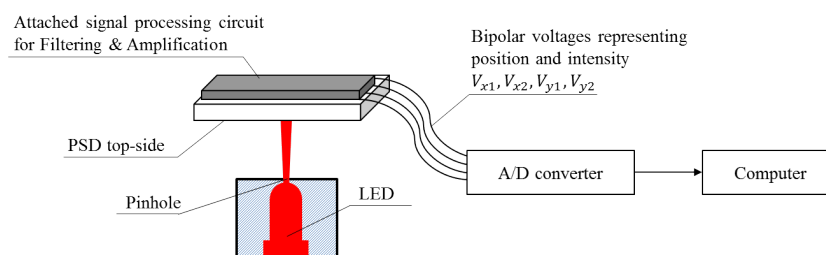


Figure 4.4: Schematic overview of the PSD position measurement system

### 4.4.1. Selecting the light modulation method

Previous research has proven the concept of position detection using a PSD under periodic light modulation [12, 17]. An important parameter in accurate position detection is the modulation frequency of the light sources. One could modulate multiple light sources at a multitude of the lowest modulation frequency and take position samples when only one beam is targeted at the PSD [17]. This method is visualized in Figure 4.5a. The main disadvantages are the increased transient time of the PSD position signal [12] and the fact that the power of each light beam needs to be reduced to prevent the PSD from saturating when all light are on simultaneously. In section 4.3 it has been measured that lowering the beam power will increase the noise level.

Instead, an alternative and more intuitive modulation method is chosen. The light beams will be modulated at the same frequency and synchronized such that only one light beam is projected on the PSD surface at any moment in time (Figure 4.5b). The modulation frequency ( $f_m$ ) of the light sources can be expressed as function of the number of light sources ( $N$ ), the number of data samples taken while each beam is projected ( $\#_{samples}$ ) and the sampling frequency ( $f_{sampling}$ ).

$$f_m = \frac{f_{sampling}}{N \cdot \#_{samples}} \quad (4.6)$$

The position signal is sampled when each LED is turned on. As mentioned before, it takes some time before a stable sensor signal is measured (transient- or settling time). The PSD settling time of  $10\mu s$  is determined using an oscilloscope. The number of samples required for reliable position detection is set to be one because of the relative long sampling time ( $\frac{1}{25kHz}$ ) compared to the sensor settling time, which results in a modulation frequency  $f_m$  of 8.3 kHz for 3 LEDs. The same readout scheme is used as visualized in Figure 4.4 but is now also includes a transistor network for modulating the LEDs. The transistor network is described in Appendix B.

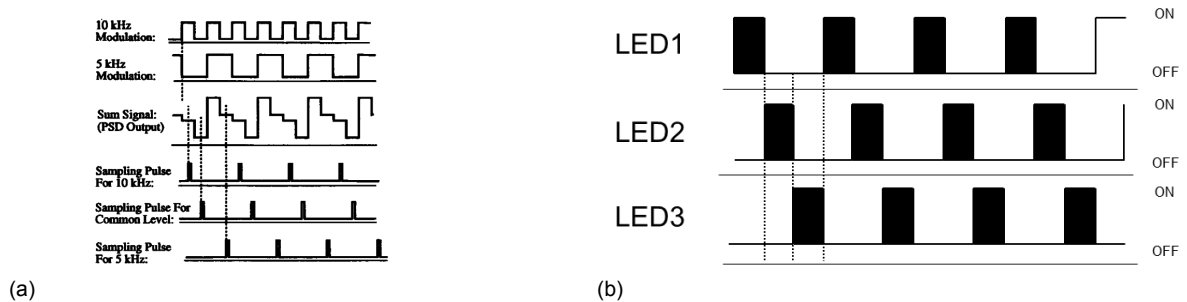


Figure 4.5: (a) Timing diagram for the synchronized signals used for sensing multiple light source positions simultaneously [17]. (b) Light beams modulated at the same frequency

## 4.5. Experimental validation of the PSD characteristics

### 4.5.1. Sensor noise sources

The measured sensor signal will pass through several sub-systems, each contributing to the noise level.

- Noise in the power supply: the PSD and the LEDs are connected to a  $\pm 15V$  and  $5V$  power supply respectively.
- Noise generated by the amplifier: the opamp and resistors used in the PSD amplifier circuit produce (thermal) noise. The magnitude of this noise source is kept low due to the high amplification factor of the currents, flowing directly from the electrodes.
- Noise generated by the sensor itself: fabrication imperfections and sensitivity to the light wavelength and optical power are the main noise sources. The optimum amount of optical power is experimentally determined described in section 4.3.
- Stray light: light sources connected to the mains cause an amplitude peak (rectified mains frequency) in the amplitude spectrum. This is kept into consideration during the stage design, by shielding the PSD from stray light.

- A/D conversion noise: the analogue to digital converters (ADC) introduce electronic noise but also quantization noise which comes from the sampling.
- Mains interference: the mains interference, also known as power line hum, is associated with the alternating current at the same frequency of the mains electricity. It shows up as an amplitude peak at 50Hz in the amplitude spectrum. Shielding and avoiding earth loops can help reducing its effect.

### 4.5.2. Determining sensor non-linearity

The signal output coming from the PSD is a direct measure of the position of the light beam. When the light beam reaches the outer borders of the PSD surface, non-linearity and signal distortions tend to increase because of the neighboring electrode contacts interfering with each other [9]. A set-up (Figure 4.6) was created for measuring the position detection linearity. A grid-scan measurement was performed by scanning the LED along a grid pattern over the PSD surface. The position signal coming from the interferometers is taken as the reference value. The reference grid pattern, visualized in Figure 4.7a, is covered in steps of  $200\mu\text{m}$ .

As expected, the non-linearity and distortions increase near the edges, indicating the maximum active working area of the PSD. The grid pattern in Figure 4.7b shows an angle between the stage and sensor axis. This is taken into account in creating Figure 4.7c, since a perfect alignment is almost impossible. From the gathered data the rotation matrix and the gain factors  $Gain_x$  and  $Gain_y$  need to be experimentally determined such that the position coordinates from the PSD can be given in SI units using equation 4.7. The PSD output is linear for more than 90% of the surface area. This limits the stage translations to  $9\text{mm}\times 9\text{mm}$ . Fitted higher order polynomials can be used to describe the whole surface and extend the translation range to  $10\text{mm}\times 10\text{mm}$ .

$$\begin{bmatrix} X_{int} \\ Y_{int} \end{bmatrix} = \begin{bmatrix} \cos(\theta) & \sin(\theta) \\ -\sin(\theta) & \cos(\theta) \end{bmatrix} \begin{bmatrix} X_{psd} \\ Y_{psd} \end{bmatrix} \cdot \begin{bmatrix} Gain_x \\ Gain_y \end{bmatrix} \tag{4.7}$$

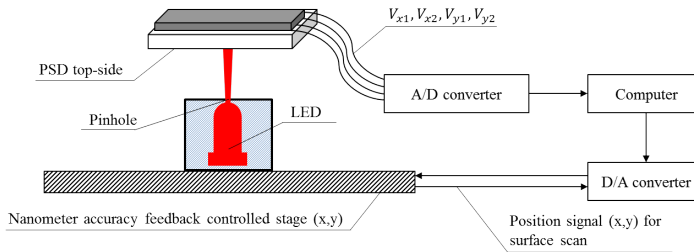


Figure 4.6: Setup for measuring PSD characteristics (non-linearity and sensor noise at different coordinates).

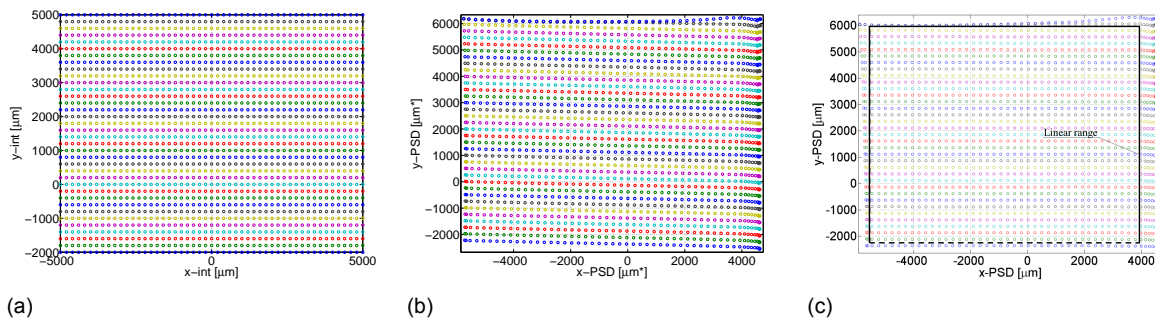


Figure 4.7: (a) Reference grid covered with an accurate feedback controlled stage (using interferometers as sensors) in steps of  $200\mu\text{m}$ , each data point is the average of 2500 samples. (b) PSD position signal measurement for a grid measurement. (c) PSD grid measurement corrected for rotation and gain error.

### 4.5.3. Measurement of sensor noise and the effect of low-pass filtering

The sensor is limited by noise which can be expressed as Gaussian distributed white noise. This was verified by measuring the noise amplitude spectrum, depicted in Figure 4.9a. The cumulative amplitude spectrum in Figure 4.9b verifies the ever increasing noise amplitude (in terms of  $3\sigma$ ) for increased frequencies. It also shows that there are no particular frequencies with increased noise amplitudes (as described in section 4.5.1). This has mainly to do with careful hardware selection and shielding from stray light.

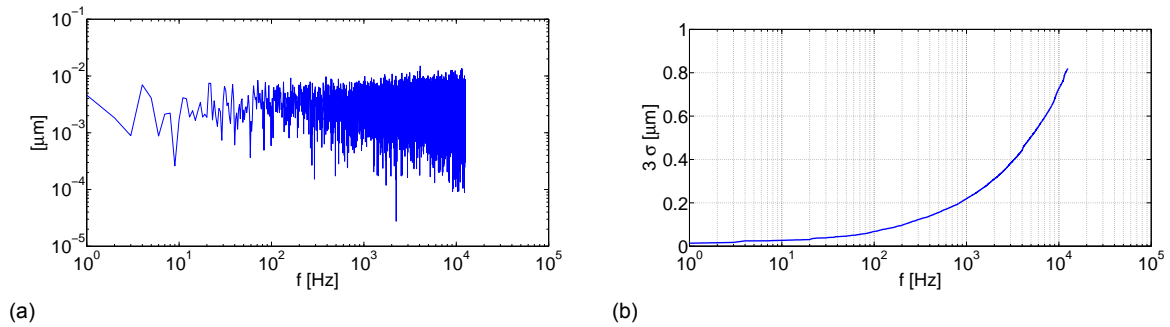


Figure 4.8

Figure 4.9: (a) PSD noise amplitude spectrum. (b) PSD noise cumulative amplitude spectrum in terms of  $3\sigma$ .

To gain more insight into the noise at different positions on the PSD surface, the same setup as depicted in Figure 4.6 is used. The light source was turned on for a specified period of time while the sensor output was recorded. This resulted in position deviation plots from which the  $3\sigma$  noise value is determined. The measurements were repeated across the surface of the PSD, providing the noise level as function of the location. The results are visualized in Figure 4.10a and b. It shows that the noise values are lowest at the center of the PSD and worsen towards the edges of the active area.

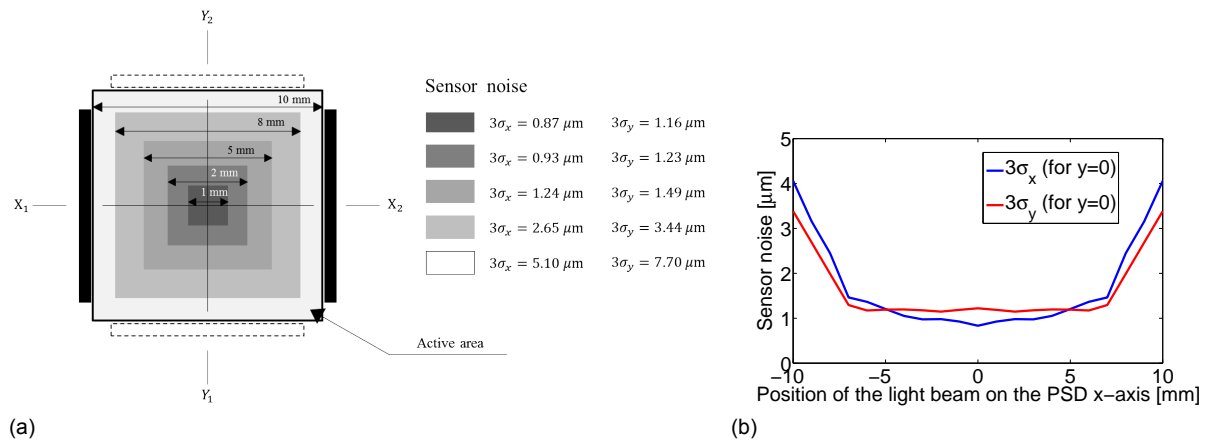


Figure 4.10: (a) Position dependent sensor noise across the PSD active area. (b) Sensor noise as function of the position along the x-axis of the PSD.

The signal-to-noise value can be significantly improved by implementing a low pass filter. For example, when the stage is moving at a high velocity, minimum noise value is not of primary importance, nor is it achievable. In order to optimize the system, it becomes necessary to vary the filtering frequency. Thus when the stage is moving over a larger distance, only coarse guidance is required meaning that the cut-off frequency of the filter can be kept high. When the stage is near its reference position, high resolution and low noise is required, since the stage has practically no velocity. In that case a filter can be applied with a lower cut-off frequency. As an example a first order low-pass filter with different cutoff frequencies is applied on the sensor noise data, resulting in lower noise value for lower cutoff

frequencies as shown in Figure 4.11. The implementation of this proposed *dynamic* filtering scheme is discussed in Chapter 6.

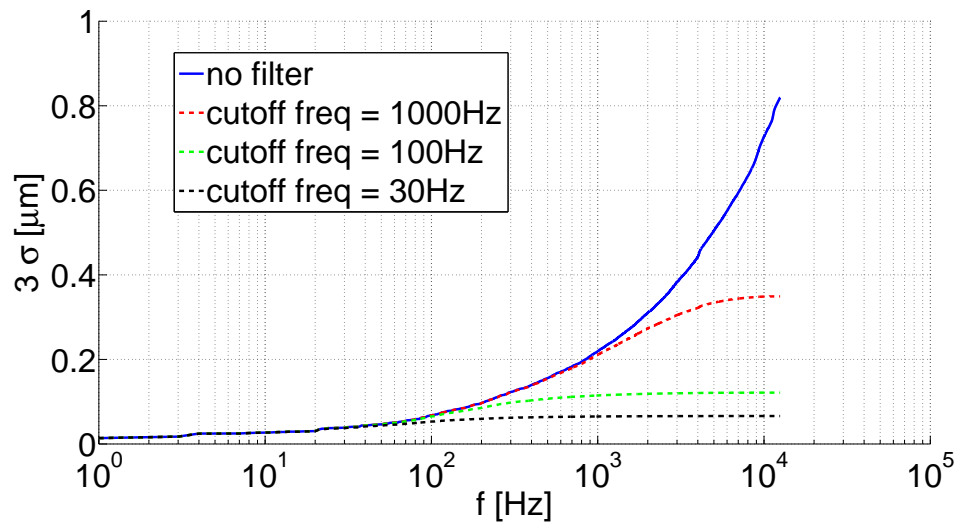


Figure 4.11: PSD noise cumulative amplitude spectrum for different first order low-pass filter cutoff frequencies.

#### 4.5.4. Drift

The performance of the PSD is limited by thermal drift noise, mainly caused by signal processing circuit attached directly behind the sensor. Figure 4.12 shows the magnitude of the sensor position drift. The sensor drift mainly limits the systems repeatability, as measured in section 7.5.

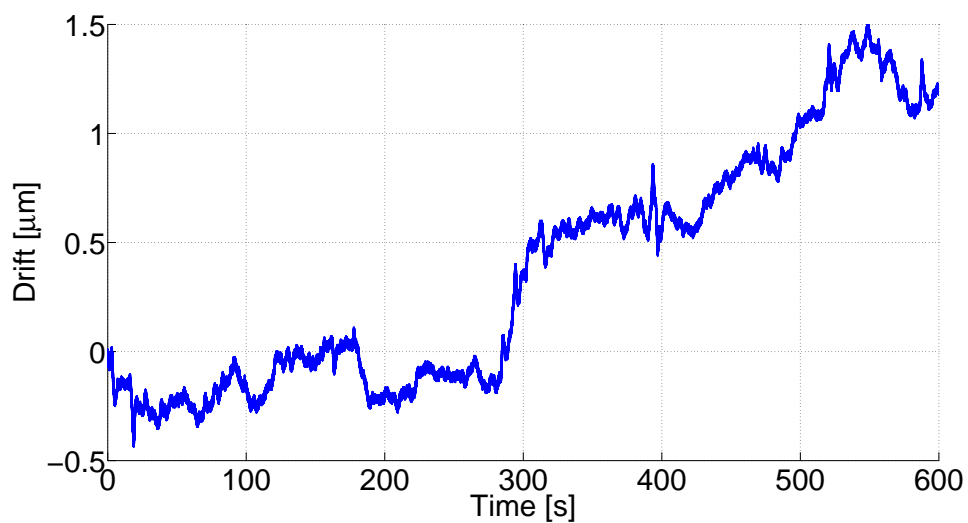


Figure 4.12: Sensor position signal drift.



# 5

## Electromagnetic Design

### 5.1. Actuation concept description

The ideal electromagnetic actuator is an actuator with a linear relation between force and current, meaning the motor constant should be independent of position, current level, speed, temperature, tolerances and environment. For this reason, Lorentz actuators are widely used within high-precision applications. Multiple concepts (i.e. actuator configurations) are taken into consideration when designing the actuator. The actuator is required to deliver forces in the  $x$ ,  $y$  and a torque in the  $\theta_z$  direction. Also, a high current to force ratio is required for delivering high forces taking constraints like heat generation and available power from the power amplifiers into account. The hard disk Lorentz actuator served as inspiration, due to the high efficiencies that can be achieved and for the fact that its design allows large rotations. The concept presented below is one that followed after many design iterations considering the desired minimum force, heat generation, manufacturability and the availability of magnets in the right shape and size. An alternative concept is presented in Appendix E.

The actuator concept visualized in Figure 5.1 can be divided in two sets each containing three coils. Commutation between the two sets enables the stage to make large rotations. The commutation process is described in detail in section 6.7. Permanent magnets are used to generate the magnetic field. The permanent magnets are fixed to the moving stage while the current carrying coils are fixed at the base. The main benefits are the wireless force transfer between the moving stage and the base and that the (majority) of the heat will be dissipated at the coils, away from the precision stage where heat is unwanted due to thermal expansion. Also the samples placed on top of the stage can be heat sensitive and should therefore be kept away from any heat source.

Figure 5.1 illustrates how forces in the  $x$  and  $y$  direction and the torque are generated when coil-set I is activated (the same working principle can be applied on coil-set II). The three coils work together to generate the forces and torque relative to the coordinate system. For each set of coils a different force transformation matrix is required to convert the force applied at each actuator location into forces and torque relative to the center coordinate system. The relation between the force generated at each coil-set and the modal forces is defined in equation 5.1 and 5.2, where  $\mathbf{F}$  is the resultant modal force,  $\Phi_{F_1}$  and  $\Phi_{F_2}$  are the force transformation matrices and  $\mathbf{F}_I$  and  $\mathbf{F}_{II}$  are the forces generated by coil-set one and two. More information regarding the transformation matrices can be found in Appendix G.

$$\mathbf{F} = \Phi_{F_1} \mathbf{F}_I \quad (5.1)$$

$$\mathbf{F} = \Phi_{F_2} \mathbf{F}_{II} \quad (5.2)$$

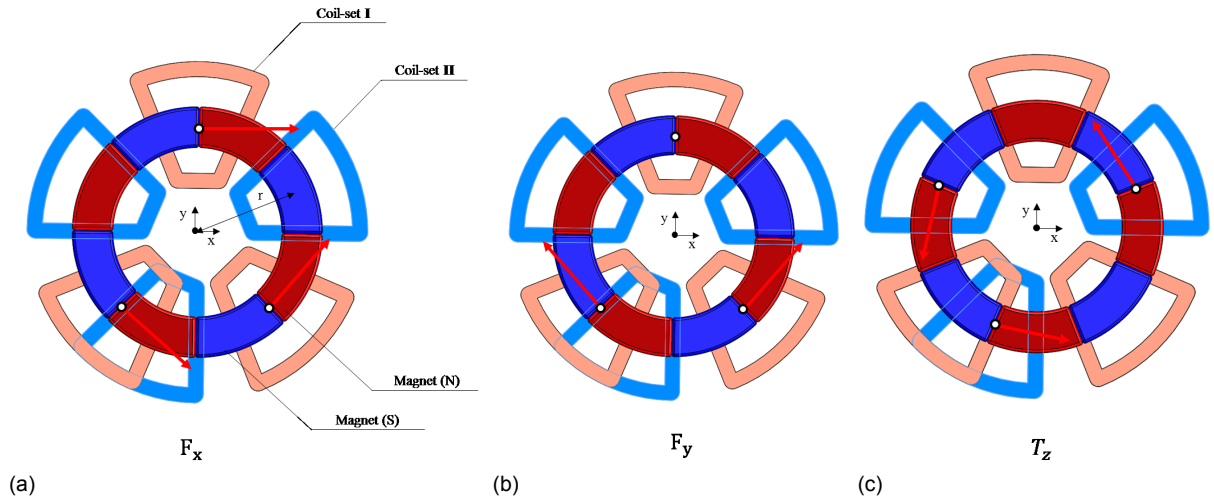


Figure 5.1: (a) Actuation concept based on the Lorentz actuation principle. Two sets of coils are used to generate forces and a torque in the  $x$ ,  $y$  and  $\theta_z$  direction respectively.

## 5.2. Magnet and coil geometry configuration

The concept visualized in Figure 5.1 uses a permanent magnet array containing 8 magnet segments next to each other with altering polarity. The array can be compared with four sets of hard disk actuators shown in Figure 5.2a. The stage has a range of  $9\text{mm} \times 9\text{mm} \times 360^\circ$  ( $x$ ,  $y$ ,  $\theta_z$ ) which means that the magnet segments and coils need to have certain minimum dimension. The selection of strong off-the-shelf permanent magnets is limited, especially when searching for segmented magnets. The magnets are therefore salvaged from old hard disk drives which met the required dimensions. The coils are designed in such a way that the return path is located inside a magnetic field with opposite polarity. The outer dimension of the coil are adjusted to the magnet dimensions (visualized in Figure 5.2b), with the objective of allowing the required translations and rotation.

The working range of the coils is larger than the width of the magnets (overhang configuration). This means that at any given time, there will be parts of the coil which produce heat due to the flowing current, without contributing to the force generation. On the other hand, smaller magnet segments at the mover means less weight that needs to be accelerated during motion.

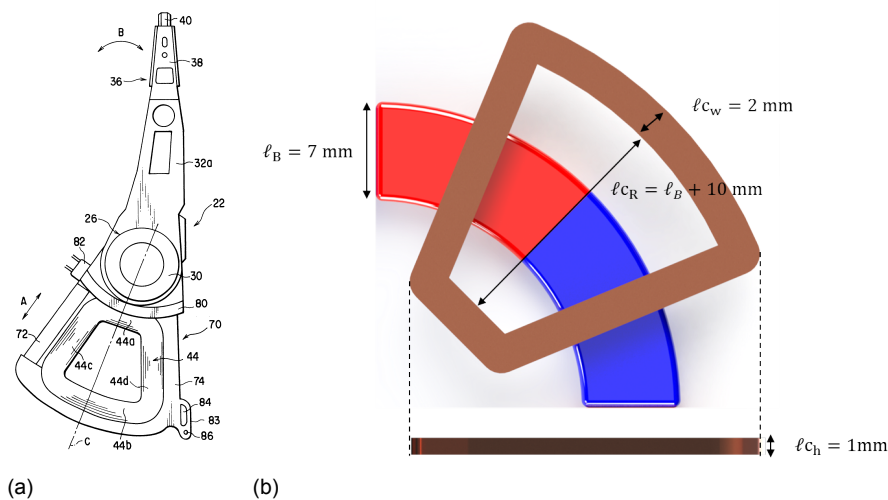


Figure 5.2: (a) Head actuator mechanism containing a current carrying coil [20]. The return path of the coil is located inside a magnetic field with opposed polarity. (b) Schematic representation of the coils used for actuating the stage.

### 5.3. Optimizing the actuator force

Given the geometrical choices made in section 5.2 we can continue with optimizing the force induced by each coil. An analytical approach is taken to optimize the actuator size and geometry. The objective is to maximize the actuator force, for a set of variables, given by:

$$\mathbf{F}_{\text{coil}} = \mathbf{B}_y \cdot I \cdot \ell_B \cdot n \cdot 2 \cdot \cos(22.5^\circ) \quad (5.3)$$

With  $\mathbf{B}_y$  the magnetic field perpendicular to the coil,  $I$  the current per coil,  $\ell_B$  the length of the wire inside the magnetic field,  $n$  the number of windings and  $2 \cdot \cos(22.5)$  because also the return paths of the coil is located inside the magnetic field under an angle. Paragraph 5.3.1 deals with the overall design of the magnetic circuit, which is further analyzed in paragraph 5.3.2 to determine  $\mathbf{B}_y$ . Finally in paragraph 5.3.3 the optimal number of windings are determined for achieving maximum force.

#### 5.3.1. Magnetic circuit design

The magnitude of magnetic flux density  $\mathbf{B}$  perpendicular to the coil ( $\mathbf{B}_y$ ) depends on many things like the magnet material, geometry, size, permeability of parts, orientation and position with respect to the coil. Two feasible magnet configurations are introduced Figure 5.3. Configuration I represents a single ring-shaped magnet array attached to a metal plate, while Configuration II represents a double magnet assembly. The magnetic circuit visualization does not represent the actual magnetic circuit (which is more complex due to the circular array configuration), but is rather used to understand the fundamental difference between the concepts.

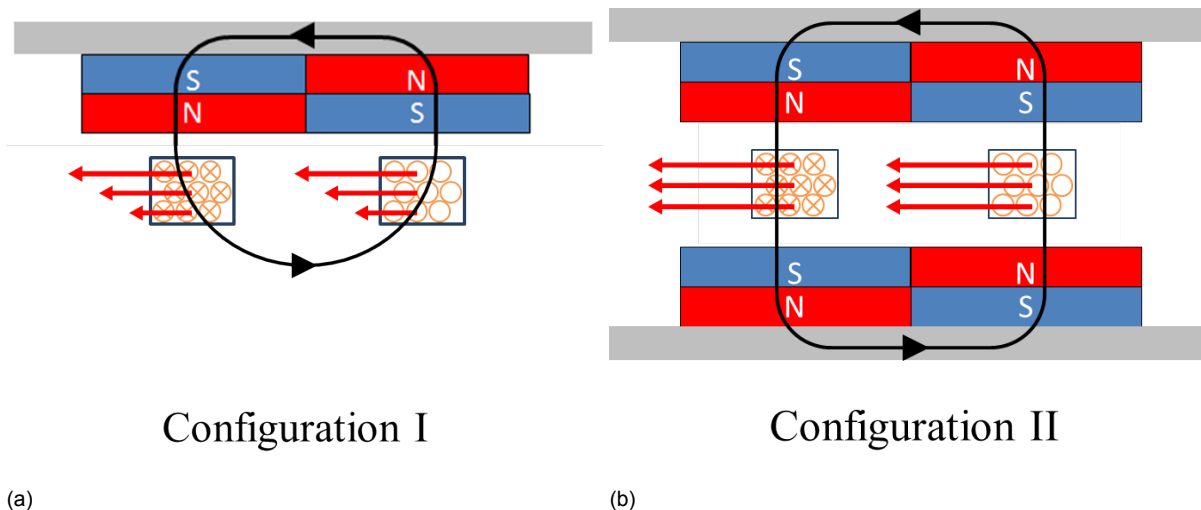


Figure 5.3: Schematic representation of the magnetic circuit when only using magnets at the top (a) or applying a double structure (b). The double structure creates a stronger and more homogenous magnetic field.

Both configurations are compared analytically. In Figure 5.4 the magnetic field strength ( $\mathbf{B}_y$ ) is plotted against the distance from the magnet surface. The graph not only shows that the magnetic field strength is 81.0% higher in configuration II, but it is also more homogenous. The mass of the moving stage will only be increased by 56.1% when choosing configuration II over configuration I. Thus the second configuration is chosen for further analysis.

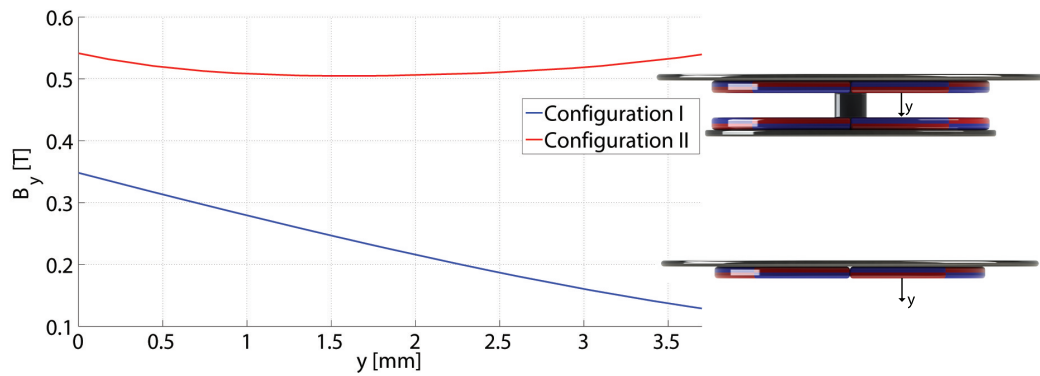


Figure 5.4: Magnetic field strength  $B_y$  at a distance  $y$  from the magnet surface for both configurations. The double magnet configuration provides a stronger and more homogenous field. The gap-size in the double-magnet configuration is around 3.5mm.

### 5.3.2. Magnetic field analysis

The double magnet configuration (II) is chosen for further analysis. A 3D COMSOL model is used to analyze the magnetic field properties. Iron plates are added to increase the strength of the magnetic field in between the magnets, thus increasing the actuator force. Figure 5.5(a) shows the magnetic flux density and the direction of the field lines in between the magnets. It can be seen that the field is homogenous before a transition phase occurs after which the polarity changes and with that the direction of the field lines.

From the cross section view in Figure 5.5(b) it can be seen that the flux density in the metal plate has increased to saturation values, which occurs around 2.2 T. Increasing the plate thickness from 1 mm to 1.5 mm and 2 mm prevents the top plate from being partly saturated. However, the mass of the stage will increase with 28.1% and 57.8% respectively while the  $B_y$  in between the magnets remains the same. An ever thinner planar will saturate over a larger area and not provide enough shielding. For that reason, the thickness of the metal plate is chosen to be 1mm. As a final test, a piece of ferromagnetic material was placed against the top plate. As expected there was hardly any reluctance force, thus it didn't stick.

Figure 5.5(c) shows the y-component of the magnetic field strength ( $B_y$ ) in between the magnets for the complete magnet array, thus the full 360°. The field strength is determined for multiple plate thicknesses with the difference in field strength being less than 0.5%. The maximum value for  $B_y$  is  $\pm 0.5$  T while the rest of the field is altering in a sinusoidal shape.

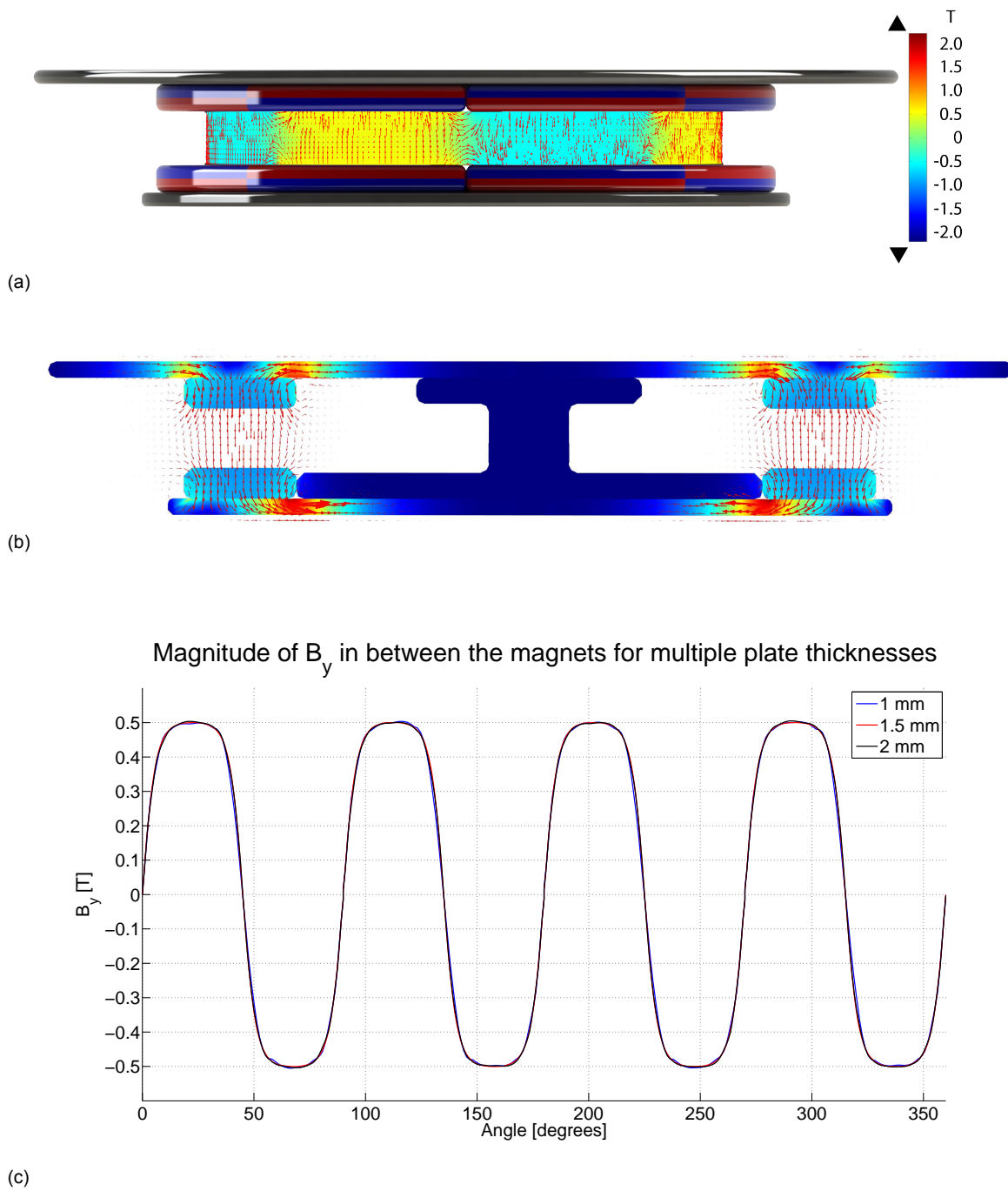


Figure 5.5: (a) Magnetic flux density and the direction of the field lines in between the magnets. (b) Cross-sectional view of the magnetic field between the magnets. (c) Change in  $B_y$  in between the magnets for the complete magnet array. The  $B_y$  is calculated for multiple plate thicknesses but difference in strength remains less than 0.5%.

### 5.3.3. Optimizing the number of windings

The outer dimensions and geometry of the coil and magnets are determined in the previous sections. The only remaining variable to be optimized is  $n$ , the number of windings, which is closely linked with the current  $I$ . The following constraints should be taken into consideration:

- The maximum temperature of the coils should not exceed  $80^\circ$ . This is limited by the demagnetization temperature of the magnets. The power dissipated per coil is:

$$Q = I^2 R_{coil} \quad (5.4)$$

This results in a temperature rise of (assuming that all the heat is dissipated by means of convection through air):

$$dT = \frac{Q}{h_{air} \cdot A_{sink}} \quad (5.5)$$

with  $h_{air}$  the heat transfer coefficient of air and  $A_{sink}$  the total surface of the coil. The coil resistance can be derived from the coil dimension:

$$R_{coil} = \frac{4 \cdot l_{coil} \cdot \rho}{\pi \cdot d_{coil}^2} \quad (5.6)$$

with  $l_{coil}$  the total coil length and  $\rho$  the electric resistivity of copper.

- The maximum current is limited by the power supply to 5A, resulting in a maximum of current of  $\frac{5}{6}$  A per coil.
- The minimum coil diameter is set to be 0.2 mm. This wire diameter is recommended by the American Wire Gauge (AWG) for the estimated current levels.

After running a MATLAB optimization algorithm for the two variables ( $d_{coil}$ ) and  $I$  while taking the constraints into account, an optimal point was found. Figure 5.6 shows a contour plot of the maximum force induced by the coil as function of  $d_{coil}$  and  $I$ . It can be seen that decreasing  $d_{coil}$  and increasing  $I$  will result in a higher force, but the temperature will increase as well. The optimal point is marked in red, for the values  $I=0.62$  A,  $d_{coil}=0.2$  mm ( $n=50$ ) resulting in a force of 0.2 N, which is more than the required 0.14N per coil.

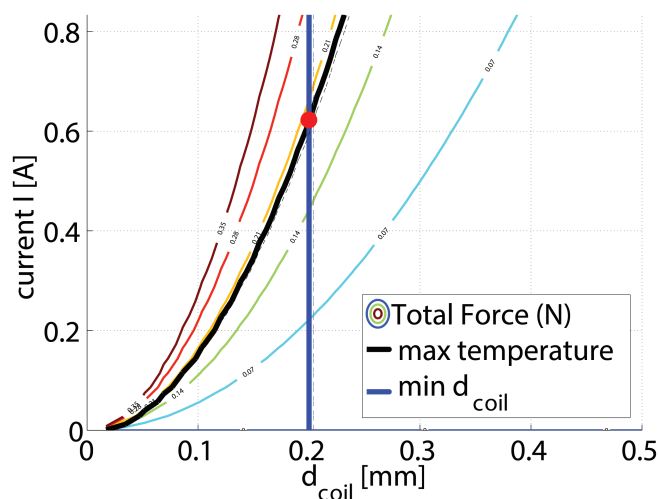


Figure 5.6: Contour plot of total force ( $F$ ) induced by one coil as function of the current ( $I$ ) and coil diameter ( $d_{coil}$ ). The active constraints which are maximum temperature and the minimal coil diameter are limiting the optimal point ( $F=0.2$  N) which is marked red.

## 5.4. Actuator modeling and validation

### 5.4.1. Temperature measurements

Temperature measurements are important for two reasons. Firstly, temperature deviations can cause expansion of certain parts of the stage and that way introduce unwanted strain. The second reason has to do with the demagnetization of the permanent magnets, which are placed very closely to the coils. Temperature measurements are performed optically using the FLIR A300 thermal camera.

In Figure 5.7(a)(b)(c) the temperature profile of a coil is shown when the currents 0.2 A, 0.5 A and 0.8 A are applied. The corresponding dissipated power is thus 0.09W, 0.55W and 1.4W respectively. It should be noted that temperature measurements for higher currents are performed for a shorter time-period in order to prevent damaging the coils. The coil temperature is plotted in Figure 5.7(d). The solid lines represent measured data which are extrapolated over time, shown as dashed lines. For each current, the corresponding maximum temperature is calculated using equation 5.4 and visualized as dashed horizontal lines.

From the plot in Figure 5.7(d) it can be concluded that the coil will reach very high temperatures, but only when reasonable high currents ( $> 0.4$  A) are applied. During normal operation, the temperature rise will remain low due to the low currents required for disturbance rejection. The large thermal rise time of approximately 45 seconds allows applying large currents for a short period of time, for example in case of a step response.

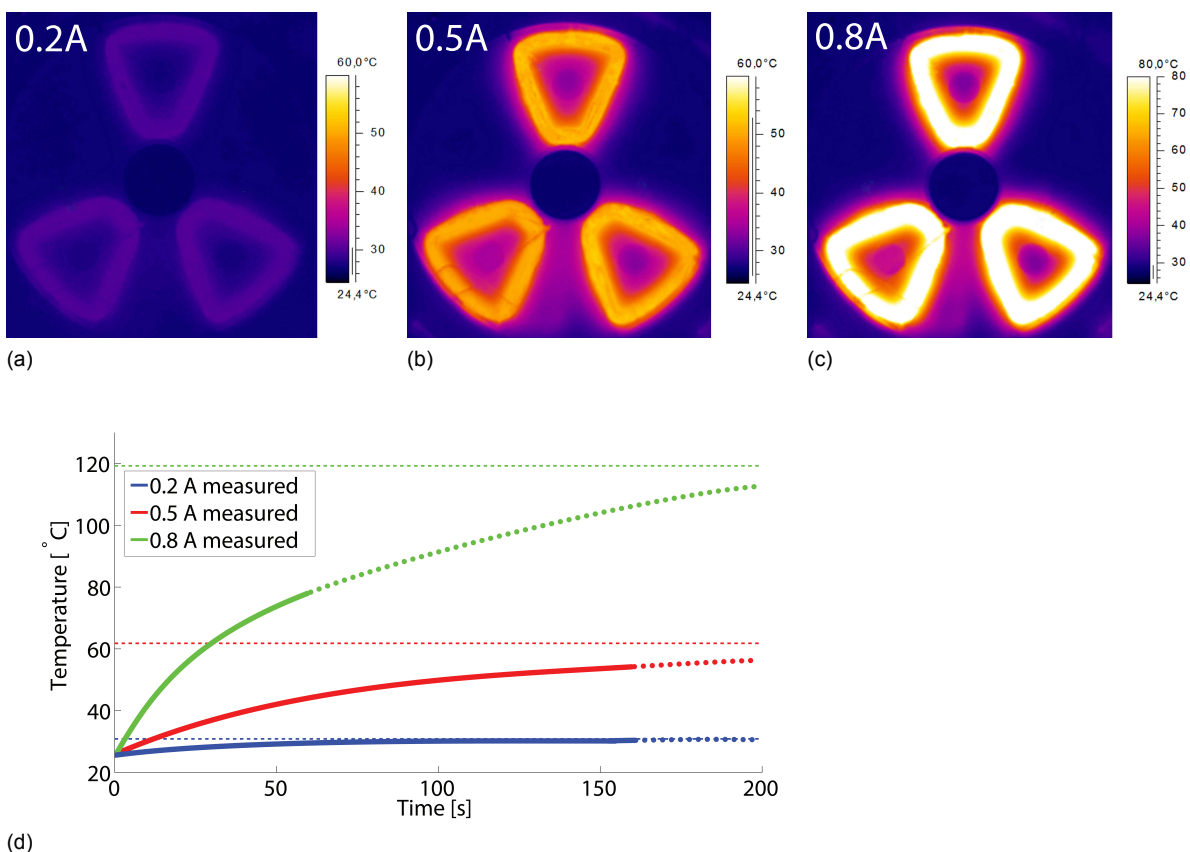


Figure 5.7: (a)(b)(c) Thermal image of the coils, measured for three currents: 0.2 A, 0.5 A and 0.8 A. (d) Temperature measurements over time for three currents (0.2 A (blue), 0.5 A (red) and 0.8 A (green)). The solid lines represent actual measured temperatures which are extrapolated over time (dashed). The temperature graphs for each current will eventually reach the predicted steady state temperature (horizontal dashed line).

### 5.4.2. Motor constant validation

The actuator force determined in section 5.3.3 should preferably be position independent. Thus the motor constant  $K_t$  should be approximately the same for all positions. To get a better understanding of the behavior a detailed 3D COMSOL simulation (model visualized in Figure 5.8a) is performed together with real measurements using the setup displayed in Figure 5.8b. To save (computational) time, only coil-1 is validated. If the results would show any unexpected results, then a full actuator validation including all six coils is necessary.

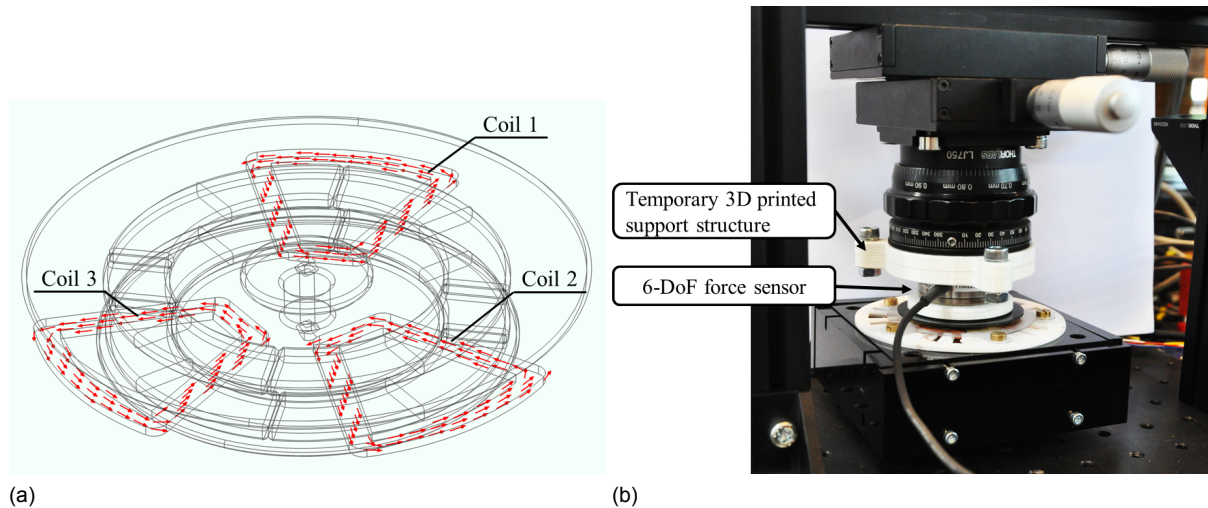


Figure 5.8: (a) COMSOL simulation of three current carrying coils inside the magnetic field, for determining the actuator force. (b) Measurement setup for measuring actuator forces and torque. A force sensor is mounted between the moving stage and a 3D printed support structure.

Figure 5.9 shows the modeled and measured motor constant  $K_t$  in the x-direction at various stage positions along the y-axis and various angles of the stage. The measured motor constant is constant within 8% over the full position range. The average error between the measured and modeled values is 11%. This is probably caused by the facts that the magnets have a different remanence, or that the coil dimension are different than modeled or that the position of the stage is slightly different due to inevitable manual adjustment errors.

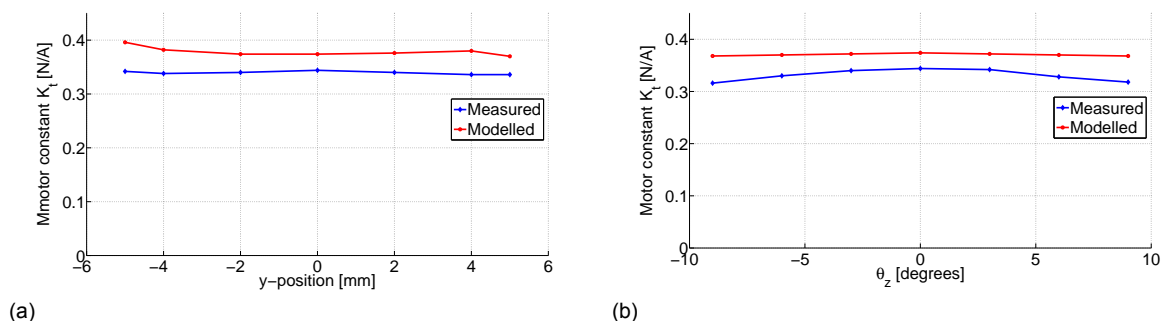


Figure 5.9: Modeled and measured motor constant  $K_t$  in the x-direction for coil-1. The measured  $K_t$  remains constant within 8% over the full position range. The measured and modeled actuator forces differ on average 11% from each other.

## 5.5. Power amplifiers

Six current amplifiers are required to convert the computer signal into the electrical current for the actuator coils. The Operational Amplifiers, pre-designed and built by Max Cafe are checked for applicability before implementation. It is important to understand the limitations of such an amplifier.

### Dynamic response limit

Figure 5.10a shows the simplified schematic of the current amplifier. The coil is visualized as an inductive load with the current  $I_o$  passing through. The amplifier gain (output current per unit input voltage) can be represented as:

$$\frac{I_o}{V_i} = \frac{R_2}{(R_1 + R_2) \cdot R_3} \quad (5.7)$$

where  $I_o$  is the output current and  $V_i$  the input voltage. The amplifier gain can be altered by changing the the voltage divider resistance ( $\frac{R_2}{(R_1+R_2)}$ ). The output current of the amplifier is measured by measuring the voltage drop over  $R_3$ , which is directly proportional with the current through  $R_3$  and moreover through the coil (load). The frequency response of the amplifier is simulated in LT-SPIICE. The simulation results in Figure 5.10b show a flat response up the resonance frequency at 5.4kHz, caused by the resonance between the coil inductance and the internal capacitance of the OpAmp. The measured response shows 16.1° phase lag at already 1kHz, but near the controller bandwidth of 100Hz, the phase lag is only 1.6°. More information regarding the amplifiers can be found in [2].

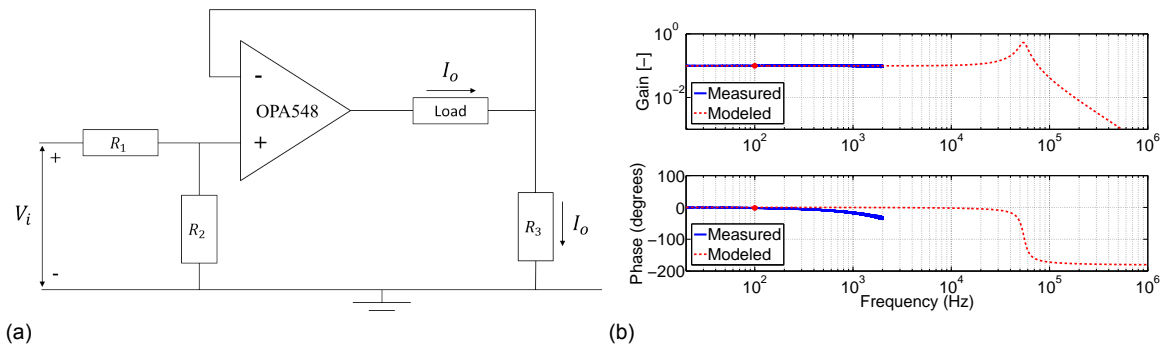


Figure 5.10: (a) Simplified schematic overview of the current amplifier. (b) Frequency response of the current amplifier connected to one actuator coil. The measured response up to 1kHz shows a phase lag of 16.1°, while the phase lag at the control frequency (red dot) is only 1.6°.

### Heat dissipation limit

The second main limitation of the power amplifier has to do with thermal limits. The power dissipated in the OpAmp can be represented as:

$$P_{diss} = V_s I - I^2 R \quad (5.8)$$

where  $V_s$  is the maximum output voltage ( $\pm 20V$ ),  $I$  the maximum current per coil which is limited to  $\frac{5}{6}A$  and  $R$  the coil resistance. The resulting maximum dissipated power is 15W, which is well within the safe operating range of the OpAmp.



## Controller Design

### 6.1. Control system overview

Figure 6.1 shows a schematic representation of the total system. The reference signal  $r$  is fed into a pre-filter block. The error between the reference signal and the actual system status is filtered and fed to the PID controller, which generates a control action (force). The controller forces are multiplied by the force transformation matrices to retrieve current amplitudes per coil. Next, based on the position of the stage, a gain will be determined for each coil-set. This ensures that the actuator force equals the desired controller force at any given angle of the stage.

The controller is designed in Matlab/Simulink and runs on a dSPACE DS-1103 system which has a 1 GHz processor and 16 bit D/A- and A/D-converters. A sampling/cycling frequency of 25kHz is used to run to complete controller.

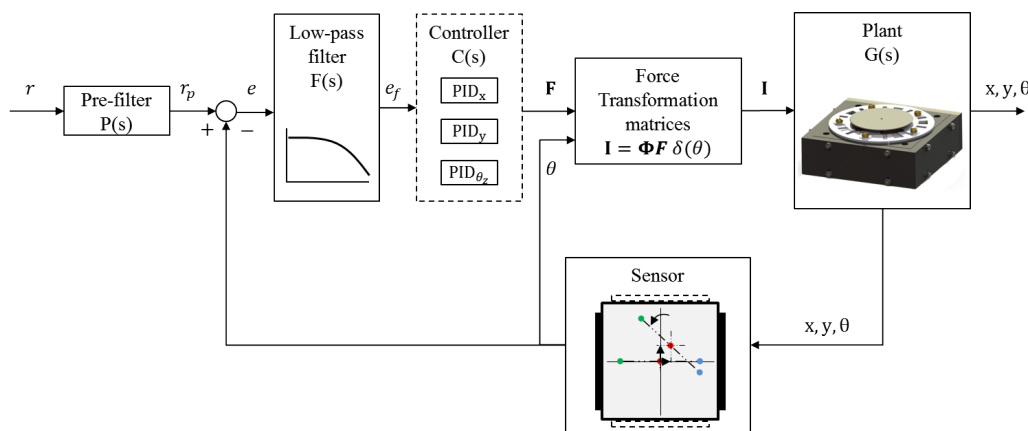


Figure 6.1: Schematic representation of the total feedback system. The reference signal  $r$  is fed into a pre-filter block. The error between the reference signal and the actual system status is filtered and fed to the PID controller, which produces the control action. Next, the corresponding currents are calculated which serve as inputs for the plant.

### 6.2. Plant and controller model

A simplified plant model is created which allows us to make predictions about the systems behavior. Since we are dealing with a moving mass (stage) and ferrofluid bearings, the system can be described like a mass-damper system as visualized in Figure 6.2. The transfer function of the system can be described as,

$$G(s) = \frac{x}{F} = \frac{1}{ms^2 + cs} \quad (6.1)$$

where  $m$  is the total mass of the moving stage and  $c$  is the damping coefficient. Initial values for the

damping coefficient are retrieved from the work performed by Simon van Veen [22], while during the system identification process in section 6.4 it was found that the coefficient is not constant, confirming his findings.

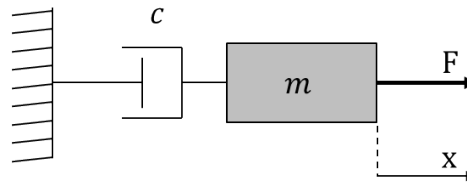


Figure 6.2: Linear plant model represented as a mass damper system. The position of the mass is denoted with  $x$ .

### PID controller

The control of the system is performed by a 'tamed' PID (Proportional-Integral-Differential) controller. It differs from a regular PID controller since the derivative action is leveled off at higher frequencies in order to prevent high frequency noise being fed back into the system. A PID controller was chosen due to the straightforward applicability and the performance that can be achieved if tuned properly. The controller can be expressed mathematically as:

$$u(t) = K_p e(t) + K_i \int e(t) dt + K_d \frac{d}{dt} e(t) \quad (6.2)$$

The control output is a sum of three terms, like visualized in Figure 6.3: the integral action takes care of any error deviations in the past, the proportional term represents the present error and the derivative term represents the future by (linearly) extrapolating the error over time. Just like the plant model, the controller can be described with a transfer function:

$$C(s) = K_p + \frac{K_i}{s} + \frac{K_d s}{\tau_f s + 1} \quad (6.3)$$

where  $K_p$ ,  $K_i$ ,  $K_d$  are the control parameters and  $\tau_f$  is the time constant of the first order derivative filter.

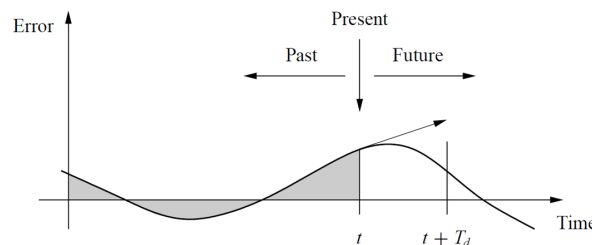


Figure 6.3: Visual overview of the PID control action over time. The integral portion of the feedback integrates the error up to time  $t$  before giving a control output. At time  $t$  the proportional term depends on the error value at that time. Finally, the derivative term estimates the error at time  $T_d$  using the rate of change of the error [1].

### 6.3. Performance specifications

In practice it is not only enough to have a stable system at a given point. The system should rather have margins of stability that describe its stability and robustness. A common way of expressing this is to use the gain and phase margins. These values tell us how much the actual system behavior can vary from the model and still be stable. The gain margin  $g_m$  is defined as the smallest increase in open loop gain before the closed loop system goes unstable, thus the increase in gain before reaching the stability limit. The gain margin can be computed from the smallest frequency (the "phase crossover frequency"  $\omega_{pc}$ ) where the phase of the open loop transfer function  $L(s)$  goes through  $-180^\circ$ . The gain margin is given by:

$$g_m = \frac{1}{|L(i\omega_{pc})|} \quad (6.4)$$

The phase margin is the additional amount of phase lag before the system reaches the stability limit. To determine the phase margin we first find the “gain crossover frequency  $\omega_{gc}$  where the gain of the open loop transfer function is unity. The phase margin can then be described as:

$$\phi_m = \pi + \angle L(i\omega_{gc}) \quad (6.5)$$

The recommended values of the margins are gain margin  $g_m = 2 - 5$  and phase margin  $\phi_m = 30^\circ - 60^\circ$  [1]. In the previous section we have described our plant with a second order transfer function. This means that the phase will never cross  $-180^\circ$ , meaning that theoretically the gain can be increased infinitely. In reality this is not the case due to unaccounted system and sensor dynamics.

## 6.4. System identification and controller tuning

### 6.4.1. System identification

The plant model in section 6.2 is a simple representation of the moving stage. In order to build a robust controller we need the plants actual frequency response. The plant is excited in the x direction with a predefined force at frequencies ranging from 10 to 500 Hz. The same procedure is applied for the y- and  $\theta_z$ -direction in Appendix F. The plant response is defined as:

$$G_x(j\omega) = \frac{x}{F_x} \quad (6.6)$$

The frequency response for the plant is determined for a force magnitude of 0.17 N and 0.3 N. From Figure 6.4 it can be seen that the damping  $c$  is different for each measurement. This is mainly caused by the larger motion amplitude and velocities that accompany an increased actuator force. At higher frequencies the plant behaves like a pure mass (-2 slope). This behavior continues up to around 190 Hz where the phase starts to decay and sensor noise and other disturbances limit the system.

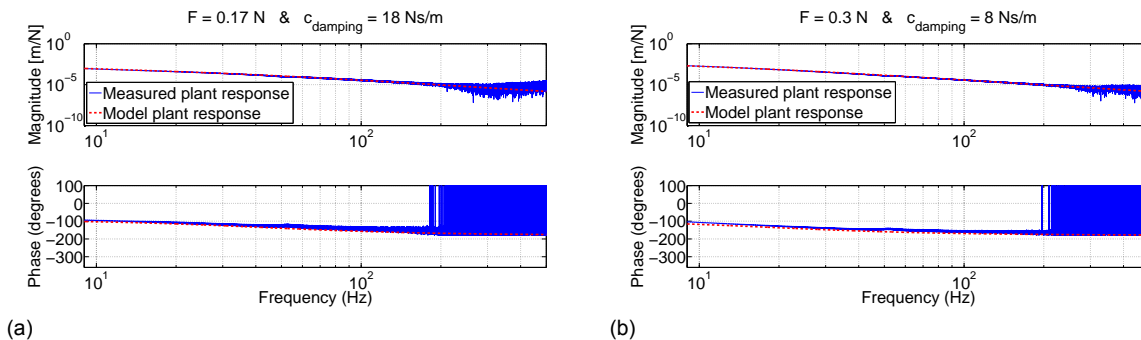


Figure 6.4: Measured and modeled frequency response of the plant for various actuation force amplitudes 0.17 N (a) and 0.3 N (b). The plant model is adjusted slightly by changing the damping parameter.

### 6.4.2. Controller and filter parameter selection

The tamed PID controller parameters are initially based on the guidelines presented by R. Munich Schmidt [11]. Figure 6.5a shows the controller response while in Figure 6.5b the open loop response  $L_x(j\omega)$  is shown. The gain and phase margin are determined based on the open loop response and visualized in the same plot. The gain margin seems to limit the system due to the increased gain magnitude at higher frequencies. It is therefore determined to implement a low pass filter to reduce the gain at higher frequencies and with that increase the gain margin without deteriorating the phase margin below the stability margins.

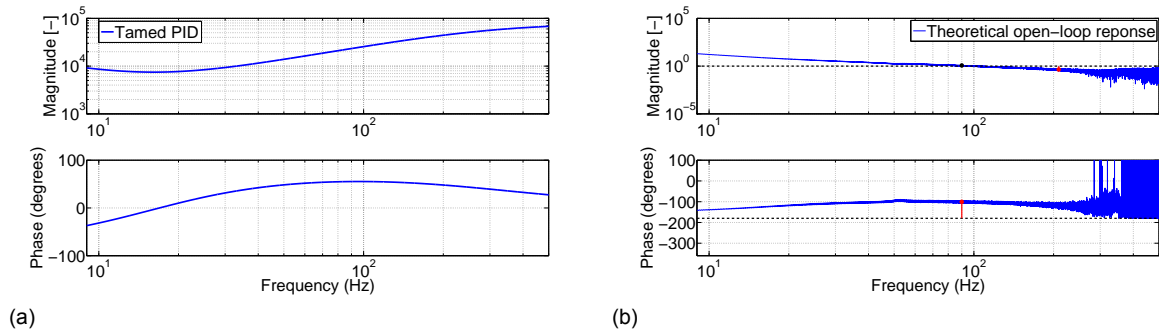


Figure 6.5: (a) Tamed PID controller response for a bandwidth of control  $f_{bw} = 90\text{Hz}$ . (b) Theoretical open loop response  $L_x(j\omega)$  where the phase margin ( $80^\circ$ ) and gain margin (2.2) are marked as red dots.

Figure 6.6 shows the modified controller response which now also includes a first order low pass filter with time constant  $\tau_{lp}$ . The open loop transfer function is the product of the controller  $C(s)$ , the mechanical plant  $G(s)$  and the low pass filter ( $F(s)$ ):

$$L(s) = C(s)G(s)F(s) \quad (6.7)$$

Implementing the filter and fine-tuning the controller parameters resulted in a 29% lower phase margin but increased the more critical gain margin with 70%. Also the control bandwidth is increased with 11% to 100Hz. The PID parameters and stability margins are summarized in Table 6.1.

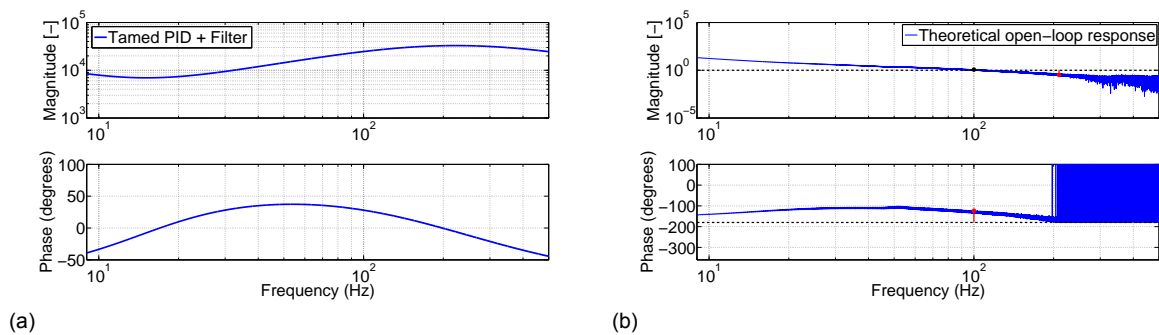


Figure 6.6: (a) Tuned PID controller and filter response for a control bandwidth of  $f_{bw} = 100\text{Hz}$ . (b) Theoretical open loop response  $L_x(j\omega)$  where the phase margin ( $57^\circ$ ) and gain margin (3.8) are marked as red dots.

Table 6.1: Controller parameters and stability margins.

Parameter	Value based on rule of thumbs	Value after manual tuning
Maximum control bandwidth $\omega_c$	90Hz	100Hz
$K_p$	$\frac{1}{3}m\omega_c^2 = 7.25 \cdot 10^3$	$\frac{1}{4}m\omega_c^2 = 6.71 \cdot 10^3$
$K_i$	$60K_p = 4.35 \cdot 10^5$	$k_p 0.1\omega_c = 4.22 \cdot 10^5$
$K_d$	$\frac{3K_p}{\omega_c} = 38.5$	$\frac{4K_p}{\omega_c} = 42.7$
$\tau_f$	$\frac{1}{3.3\omega_c} = 5.36 \cdot 10^{-4}$	$\frac{1}{2.5\omega_c} = 6.37 \cdot 10^{-4}$
$\tau_{lp}$	—	$\frac{1}{2\omega_c} = 7.96 \cdot 10^{-4}$
Phase margin $\phi_m$	$80^\circ$	$57^\circ$
Gain margin $g_m$	2.2	3.8

### 6.4.3. Closed loop response

The closed loop response is firstly calculated using experimental plant response data combined with the designed controller. The theoretical close-loop response is given by:

$$T(j\omega) = \frac{CGF}{1 + CGF} \quad (6.8)$$

From Figure 6.7a it can be seen that the theoretical close-loop response is different from the measured close-loop response visualized in Figure 6.7b. The main difference the theoretical and measured response is the “resonance” peak at the control frequency of 100Hz. Also the phase change is not as gradual as expected. The close-loop response was measured by applying a sinusoidal reference input to the system with increasing frequency and an amplitude of  $10\mu m$ . This amplitude of motion differs from the amplitudes that where observes during the system identification. The peak in Figure 6.7b can be explained with the fact that the damping variable  $c$  was lower during the close-loop measurements than when the system identification was performed. To compensate for this behavior a pre-filter is added to the system, which will be described in section 6.5.

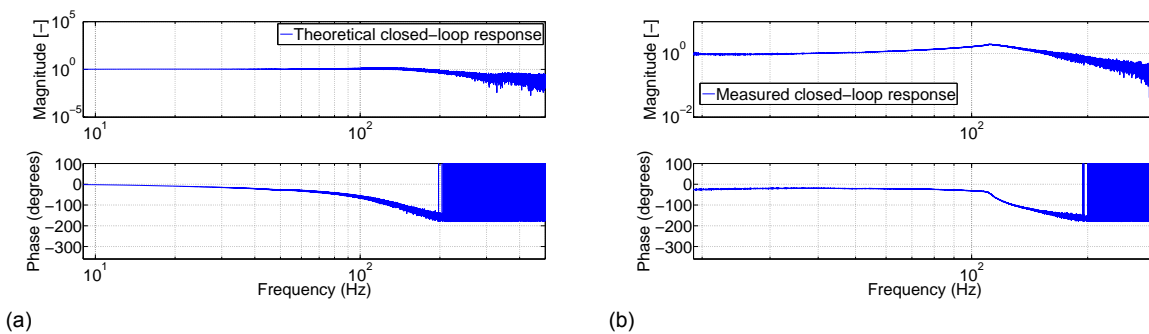


Figure 6.7: (a) Theoretical closed loop response based in the measured plant response and modeled controller response. (b) Measured closed-loop response.

## 6.5. Pre-filter design and implementation

The validated closed-loop response discussed in section 6.4.3 requires some sort of input pre-regulation to make the system response as flat as possible up-to the desired frequency. There are several methods of addressing this issue, which include implementing a pre-filter or feedforward control. The pre-filter only involves modifying the input reference value whereas feedforward control also requires access to the actuator input or controller output. The feedforward model required extensive knowledge on the variable ferrofluid damping  $c$  with respect to the step size and other factors of influence. Researching these effects is beyond the scope of this thesis but could improve the systems performance.

Using the pre-filter  $P(s)$  the closed-loop response can be adjusted. The adjustment includes flattening the unevenness in  $T(j\omega)$  in the working frequency range. Thus the pre-filter can be used in such a way that  $P(j\omega)T(j\omega) = 1$ . However, at higher frequencies the sensor noise dominates and one should also be careful not to saturate the actuators. Thus the product of  $|P(j\omega)| \cdot |T(j\omega)|$  should be kept sufficiently small at higher frequencies.

By analyzing the closed-loop response in Figure 6.7b it can be seen that the unevenness in  $T(j\omega)$  can be compensated for by applying a notch filter. Thus  $P(j\omega)$  has the shape of a notch filter which is tuned to flatten the response of  $T(j\omega)$  at lower frequencies, while at higher frequencies it has the shape of a low-pass filter. The frequency response of the pre-filter  $P(j\omega)$  is shown in Figure 6.8 as well as the measured closed-loop response  $T(j\omega)$  and the compensated system response  $P(j\omega)T(j\omega)$ .

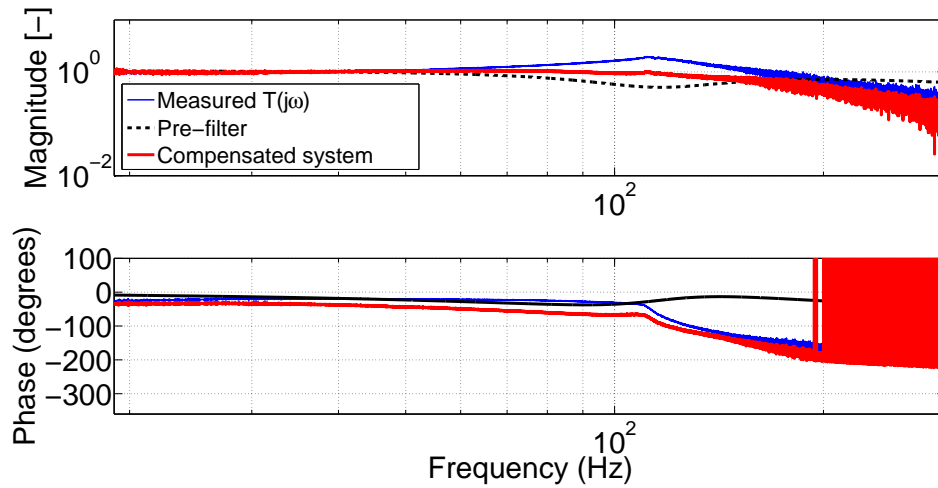


Figure 6.8: Frequency response of the measured closed-loop response  $T(j\omega)$  (blue line) which is compensated for by the pre-filter  $P(j\omega)$  (dashed black line) resulting in the compensated system response, namely the product of  $P(j\omega)T(j\omega)$  (red line), showing a more flat response in the working frequency range.

To demonstrate the effect of the pre-filter a step input is applied to the system. Figure 6.9 shows the system response with and without the pre-filter. It can be noticed that the pre-filter has no effect on the settling time, but rather smoothen the systems behavior.

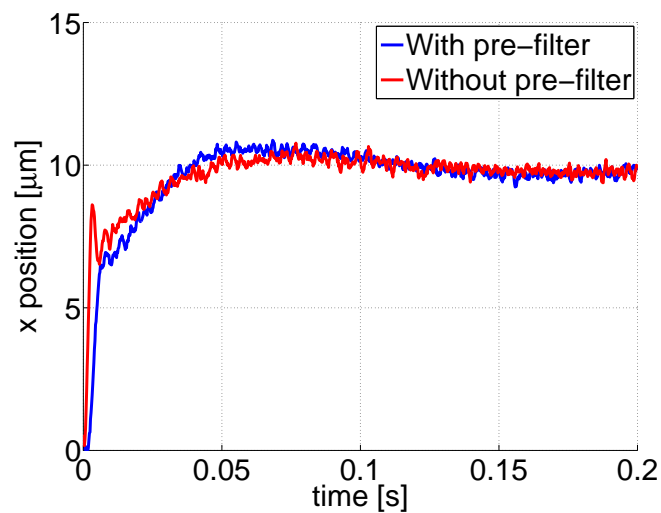


Figure 6.9: Step response of  $10\mu\text{m}$  in the x-direction, with and without the pre-filter. The pre-filter seems to smoothen system step response.

## 6.6. Integral windup and its effect

The Lorentz actuators used in the system have a maximum force that they can safely deliver. This force is mainly limited due to the maximum current that can be applied and the heat generation. The actuator output is thus limited. When the controller reaches this limit, the loop is broken and the system behaves like an open-loop since the actuator output will remain at the limited value. When this happens, the integrator error tends to accumulate and remain large even when the error is small. It takes some time before the integrator value is decreased causing a worse step response for example.

To deal with the detrimental windup effects an anti-windup function is added to the controller. The *backcalculation* anti-windup scheme as illustrated in Figure 6.10a is implemented to avoid windup. Basically an extra feedback path is created by subtracting the controller output from the saturation limit which creates an error signal  $e_s$ . The anti-windup scheme tries to keep  $e_s$  at a minimum by feeding the product of  $e_s$  times a constant  $k_t$  to the input of the integrator. The error  $e_s$  is zero in case the actuator output is within the saturation boundaries. The constant  $k_t$  is manually tuned, resulting in different step responses for different values of  $k_t$  as visualized in Figure 6.10b. A suitable value for  $k_t$  seems to be  $\frac{1}{T_i}$  where  $T_i = \frac{k_p}{k_i}$ , whereas lower values will cause a lower overshoot and high  $T_i$  values can even induce undershoot.

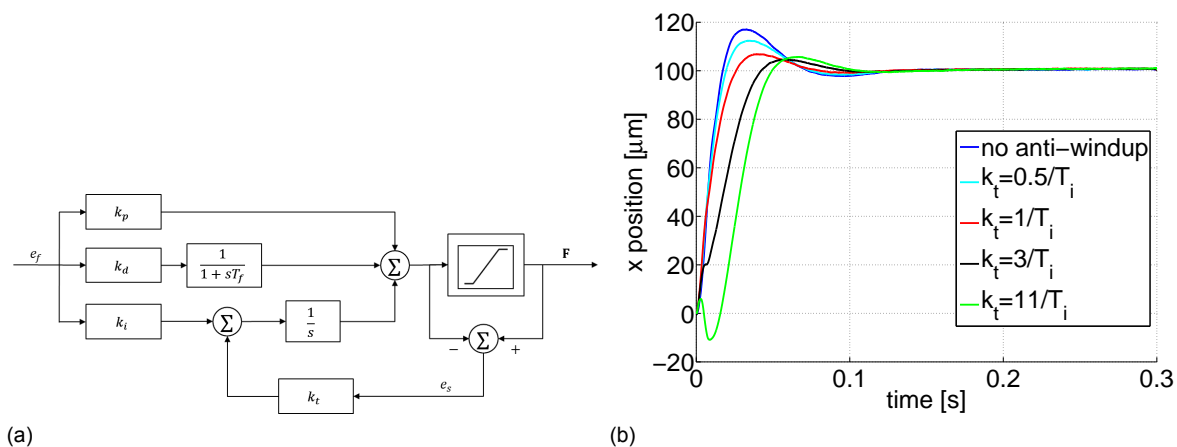


Figure 6.10: (a) Tamed PID controller with anti-windup scheme. The error  $e_s$  is built up when the controller output exceeds the saturation limit. The input of the integrator ( $\frac{1}{s}$ ) can be described as  $e_f \cdot k_i + e_s \cdot k_t$ . (b) Step response of  $100 \mu m$  in the x-direction for different values of  $k_t$ .

## 6.7. Commutation between the actuator sets

Commutation takes place when a coil-set is reaching a magnetic field region where the field strength is decreasing. An analytical approach is taken for determining the commutation profile. The field analysis in Figure 5.5c shows that the field strength remains 0.5T for a substantial period of time before altering polarity. Thus when a coil-set is within this region it should be fully activated. The disk-shaped visualization in Figure 6.11a shows when each coil-set is active. Commutation between the two coil-sets takes place gradually in order to prevent sudden shocks in the system. The commutation profile indicating the gain of each coil-set is created by linearizing the field analysis results into the profile shown in Figure 6.11b. This profile is implemented as a look-up table in the control scheme.

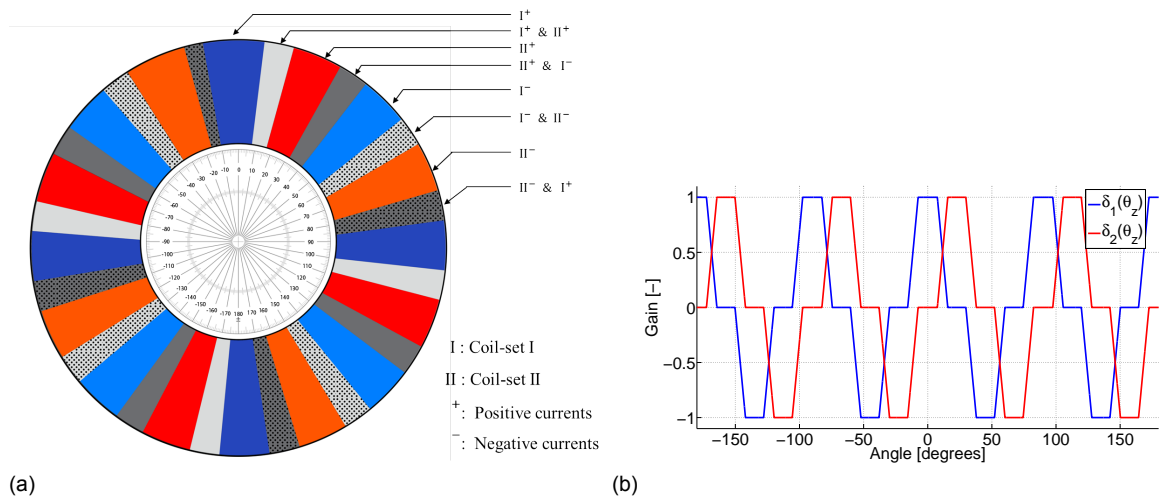


Figure 6.11: (a) Visual overview at which angle each coil-set is active. (b) Coil-set gain ( $\delta_1$  and  $\delta_2$ ) at each corresponding angle.

## 6.8. Proposed hybrid control for better position accuracy

In paragraph 4.5.3 it was suggested to filter the sensor signal more when the stage was required to stay at one position and apply less filtering when a fast position response is required for example in case of a step motion. The control scheme presented in Figure 6.1 can be extended with another controller and filter. This new control loop can be tuned for a higher positioning accuracy enabled by a more filtered sensor signal and lower control bandwidth. This allows the system to switch between a *stiff* controller for fast response times and a *compliant* controller for better positioning accuracy. The extended controller scheme is presented in Figure 6.12. Due to time restrictions this control scheme is not extensively tested but preliminary results showed a decrease in sensor noise and with that an increased positioning accuracy. However, the system is more *vulnerable* for ground vibrations (due to the lower bandwidth), thus it is recommended to use a vibration isolation table.

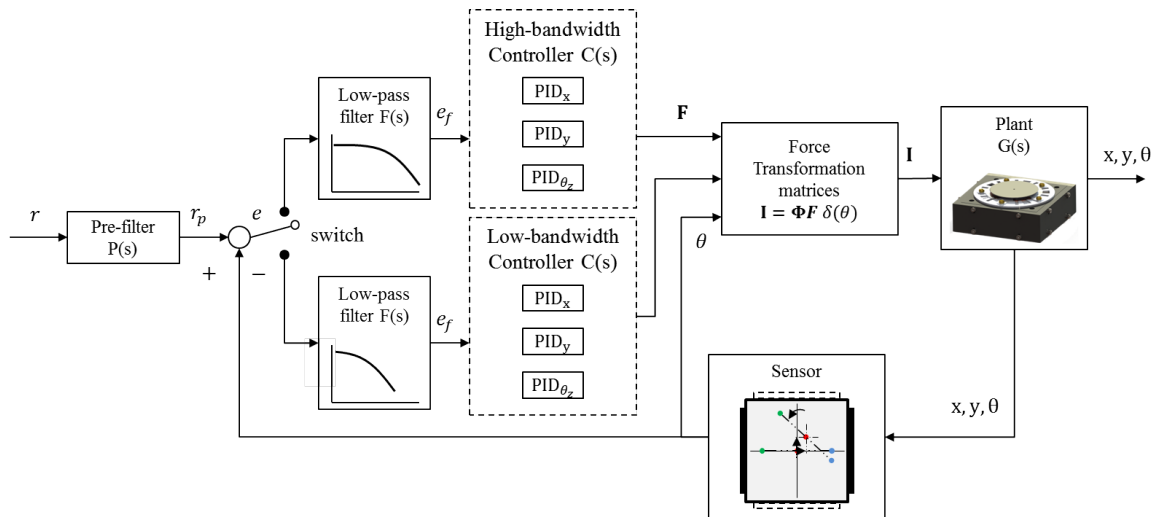


Figure 6.12: Schematic representation of the hybrid feedback system including an additional controller for better positioning accuracy at standstill.

## Performance measurement

### 7.1. Ferrofluid bearing stiffness measurement

One of the main concerns when using ferrofluid bearings is the relatively low stiffness. Simon van Veen showed in his master thesis [22] that a vertical stiffness of  $8 \frac{kN}{m}$  can be achieved with one magnet comparable of size with the magnets used in this work. It is out of the scope of this master thesis to fully predict and optimize the bearing load capacity and stiffness, yet the design choices made in section 3.2.3 were aimed to increase the stiffness and load capacity. A stiffness measurement is performed in order to quantify the bearing stiffness for the complex magnet configuration. The measurement setup is shown in Figure 7.1a. Three capacitive sensors measure the stage's change in height while the force on the stage is increased. From the graph in Figure 7.1b it can be concluded that the ferrofluid bearing stiffness seems to be linear within the range of the capacitive sensors. The measured vertical stiffness is  $76.2 \frac{kN}{m}$ .

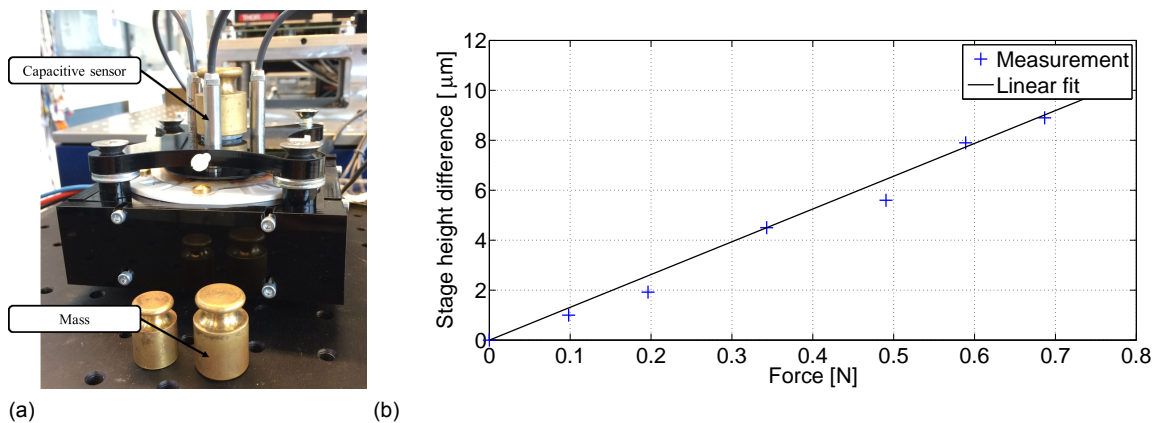


Figure 7.1: (a) Measurement setup, including three capacitive sensors, for measuring the vertical ferrofluid bearing stiffness. (b) Vertical stiffness of the ferrofluid bearings seems to be linear within the range of the capacitive sensors used. The stiffness measured is  $76.2 \frac{kN}{m}$ .

### 7.2. Step response

The step response gives a good indication of the system performance. Firstly because a faster step response will benefit the end user (higher throughput). The step response also contains an infinite range of frequencies, thus it gives a good indication of the overall stability. The system behaves identical in the x- and y-direction, thus only the results in the x-direction are shown. Steps in rotational direction  $\theta_z$  are performed for small angles which do not require commutation between the two coil-sets as well as large angles which do.

### 7.2.1. Step response in the x-direction

The step response is measured for multiple step sizes. According to the requirements, the stage should be able to perform a step of  $100\mu\text{m}$  in 0.1 seconds. Thus the settling time, which is defined as the time required for the response curve to reach and stay within a range of 2% of the final value, should be below 0.1 seconds for a  $100\mu\text{m}$  step. In Figure 7.2 the step response for a step-size of  $100\mu\text{m}$  and  $1000\mu\text{m}$  are shown. As slight overshoot can be observed after which the position reaches the reference position without any oscillations (even in case of a large step-size of  $1000\mu\text{m}$ ). The settling times are 0.098 seconds and 0.185 seconds for the  $100\mu\text{m}$  and  $1000\mu\text{m}$  step respectively.

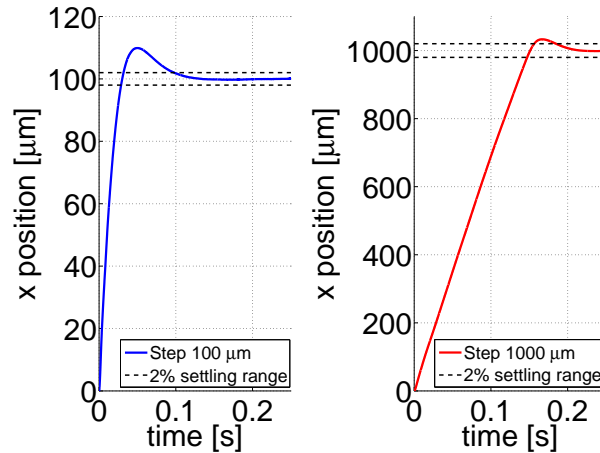


Figure 7.2: Step response in the x-direction with a magnitude of  $100\mu\text{m}$  (blue line) and  $1000\mu\text{m}$  (red line).

### 7.2.2. Step response in rotational direction

The main difference between linear and rotation steps is that for large rotational steps commutation between the coil-sets is required. In Figure 7.2 the rotational step response for a step-size of  $1^\circ$ ,  $10^\circ$  and  $60^\circ$  are shown. All three response look similar: steady acceleration until the reference position with a slight overshoot and stable settling response. Below each position response plot, the gain plot for both coil-sets is shown ( $\delta_1$  &  $\delta_2$ ). For a step of 1 degree, only coil-set one is required, while for a step size of 10 degrees, coil-set 2 is also activated and remains active together with coil-set 1. The final plot, for a step-size of 60 degrees shows that the gains vary rapidly in order to create a smooth and stable response.

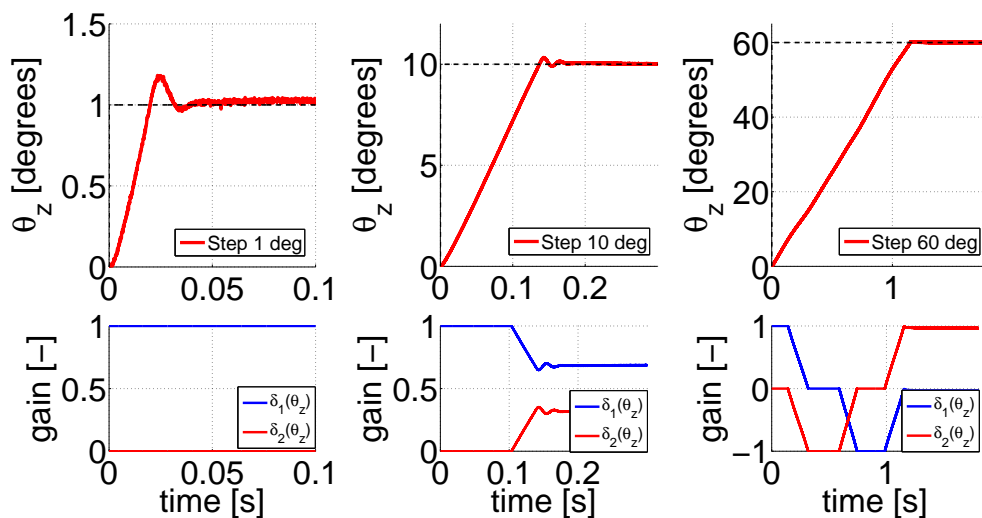


Figure 7.3: Rotational step response with a magnitude of 1, 10 and 60 degrees.

### 7.3. Sensitive for tilt

Just like with many other mechatronic systems, the sensing part is located at a different location than the desired point of measurement. In our case the LEDs and sensor are located underneath the metal plate, thus making it sensitive for angular errors. A tilt measurement is performed using the same setup as visualized in Figure 7.1a which includes three capacitive sensors. The stage is actuated by a step input in the x-direction with a magnitude of  $100\mu\text{m}$  and the tilt around the y-axis ( $\theta_y$ ) is measured. In Figure 7.4a it can be seen that the tilt increases and decreases with the acceleration of the stage. The maximum  $\theta_y$  measured is 0.02 mrad. The displacement error can be calculated using the following equation:

$$\epsilon_{abbe} = l_{arm} \sin(\theta_y) \quad (7.1)$$

where  $l_{arm}$  is the distance between the surface of the metal top-plate and the PSD. The maximum angular error  $\epsilon_{abbe}$  is  $0.5\mu\text{m}$ , as visualized in Figure 7.4b. It should be noted that this maximum error is only present during the acceleration period, which is a part of the motion where measurement errors are not critical in our case. For systems that need to follow a trajectory the measurement system must be placed in line with the moving object or the unwanted angular motion should be compensated for in a different way. For our system, this is not the case, meaning that the error has no significant impact of the stage's positioning accuracy.

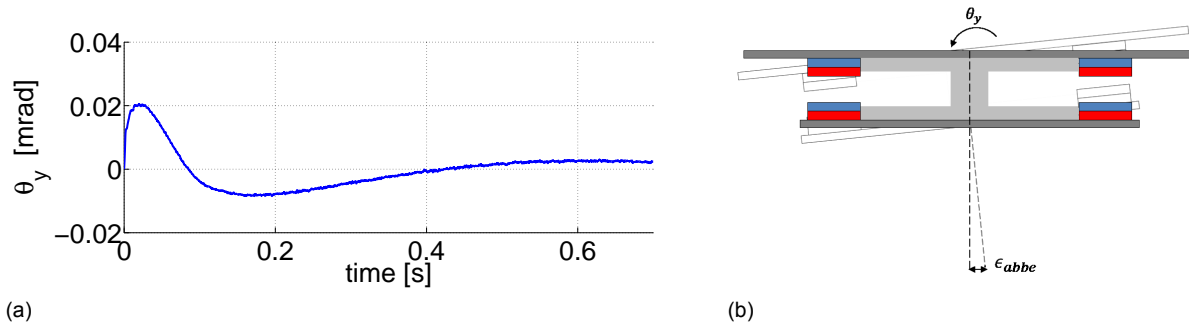


Figure 7.4: (a) Tilt measurement around the y-axis ( $\theta_y$ ) for a  $100\mu\text{m}$  step in the x-direction. (b) Visual representation of the maximum abbe error occurring when the stage accelerates.

### 7.4. Large angular reference input

In order to demonstrate the large angular movement capability of the stage, a sinus signal input is inserted as reference signal. Multiple commutation variations are required in order to complete the rotation between  $90^\circ$  and  $-90^\circ$ . The reference and measured signal are shown in Figure 7.5, together with the gain for each coil-set. From the measured signal it can be seen that the stage is very well capable of following a smooth large input signal.

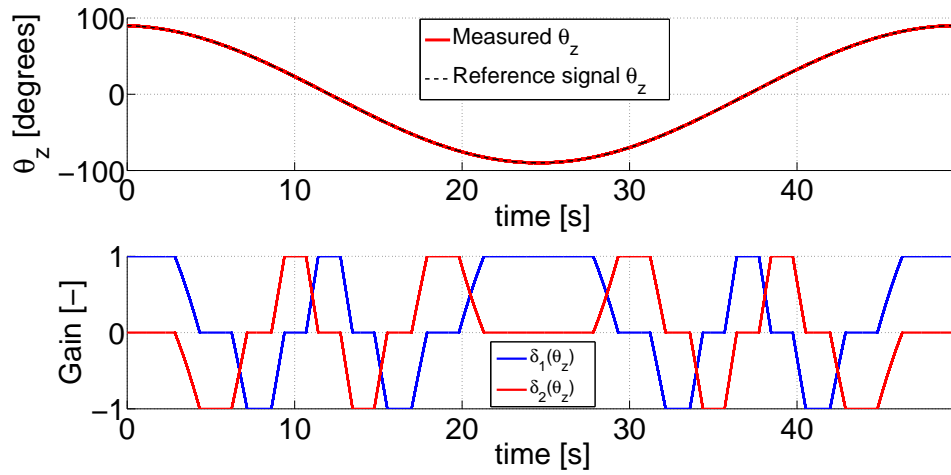


Figure 7.5: Measured  $\theta_z$  for a sinus shaped reference input between  $90^\circ$  and  $-90^\circ$ . The bottom graph shows the coil-set gains at each moment in time.

## 7.5. Repeatability

To check the repeatability of the system, the results of 50 consecutive step responses are analyzed. An algorithm is written that allows the stage to automatically makes 50 steps of  $100\mu\text{m}$ , like shown in Figure 7.7a. The position of the stage is verified using the nanometer accuracy interferometers displayed in the measurement setup in Figure 7.6. The error between the desired position and the measured position by the accurate interferometers is used as input for the probability density function in Figure 7.7b. The position error seems to have a normal distribution, with a standard deviation of  $\sigma = 0.56\mu\text{m}$ . The position find-back error is mainly caused by the sensor noise and thermal drift.

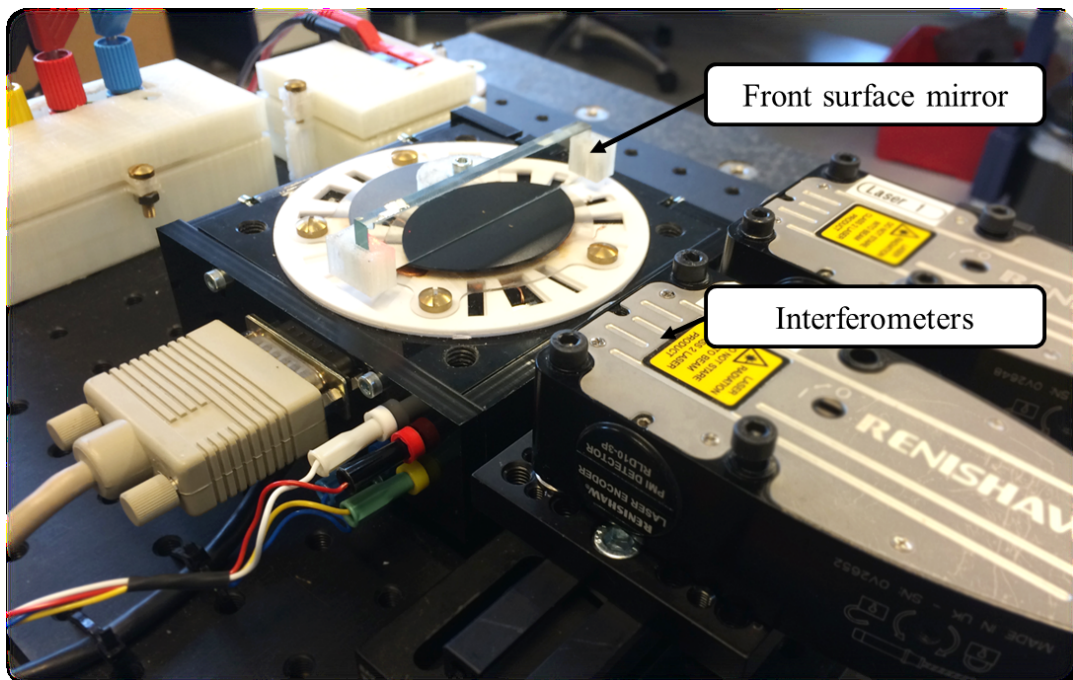


Figure 7.6: Setup used for measuring the repeatability and position stability. Two interferometers are used to measure the  $x$ - and  $\theta_z$  motion of the stage using the 'front surface mirror' mounted on the stage.

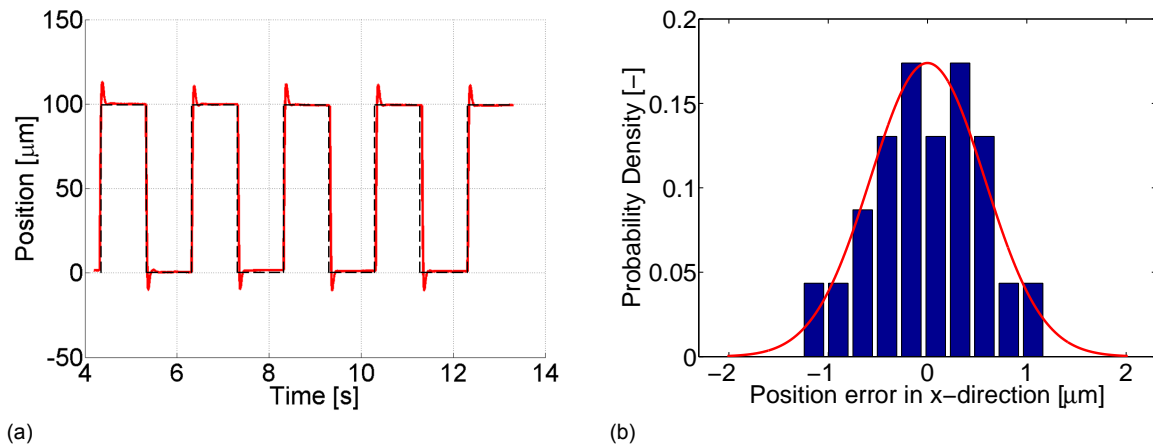


Figure 7.7: (a) Steps of  $100\mu\text{m}$  used for measuring the repeatability, by analyzing the difference between desired position and the measured position by the accurate interferometers. (b) Probability density function of the 'find-back error' with a standard deviation of  $\sigma = 0.56\mu\text{m}$ .

## 7.6. Position stability

Once the stage is in position it should remain there while rejecting disturbances as good as possible. A smaller position error means that higher lens magnifications can be used for example. The position of the stage is measured for 10 seconds in the x- and  $\theta_z$  direction using the same measurement setup displayed in Figure 7.6.

In Figure 7.8a the probability density function of the servo error in the x-direction is shown, with a standard deviation of  $\sigma = 67\text{nm}$ . The angular error has a standard deviation of  $\sigma = 0.05\text{mrad} = 0.0009^\circ$ , shown in Figure 7.8b.

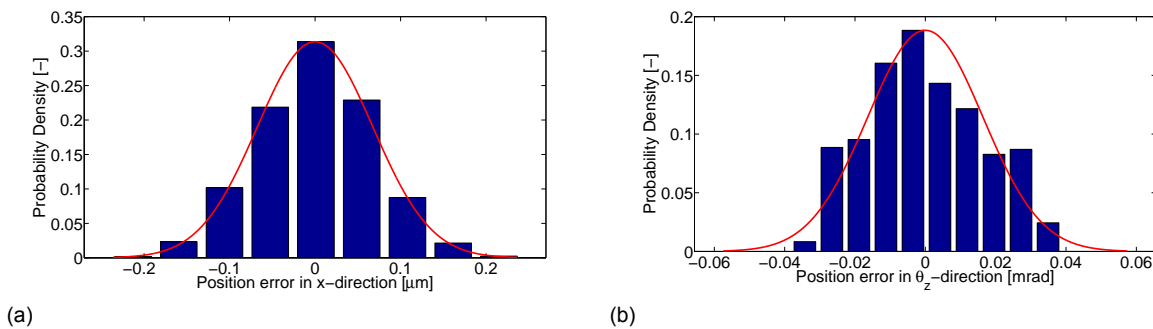
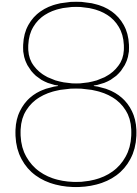


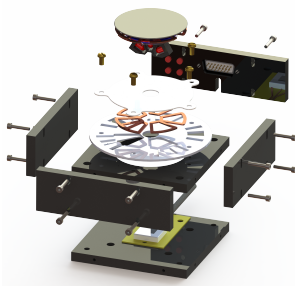
Figure 7.8: (a) Probability density function of the position error in the x-direction with a standard deviation of  $\sigma = 67\text{nm}$ . (b) Probability density function of the position error in the  $\theta_z$ -direction with a standard deviation of  $\sigma = 0.05\text{mrad} = 0.0009^\circ$ .



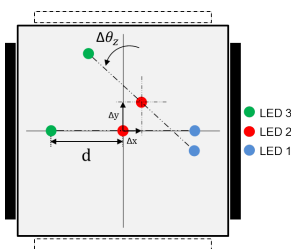


## Conclusions

In this thesis a novel approach for accurately positioning a 3 DoF planar stage is researched and implemented. The stage can complete a full rotation and has a translation range of 9 mm x 9 mm. Planar positioning accuracies of  $0.2\mu\text{m}$  ( $3\sigma$ ) in the x/y-direction and  $0.15\text{mrad}$  ( $3\sigma$ ) in the  $\theta_z$ -direction are achieved. The unique features of combining a translation and rotation stage in one compact and cost effective system make it one of a kind and nothing comparable is found on the market.



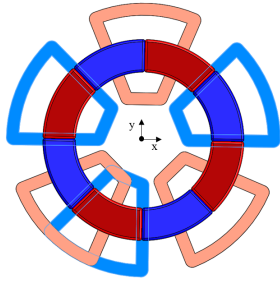
The demonstrator is built in-house using simple but effective manufacturing processes like laser-cutting and 3D-printing. These methods allow greater design flexibility and decrease the production time in comparison to common manufacturing processes like milling. The control bandwidth of the system is not limited by the mechanical resonances, but rather by the sensor noise.



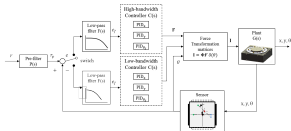
By sequentially modulating three light beams on the PSD surface, three position signals equivalent to the position of the light beams is retrieved. A sensing algorithm has been developed for sampling and converting these sensor signals into planar position data: x, y and  $\theta_z$ . The rotation range of the mover is not limited by the sensor, instead is it limited by the wires attached to the mover for controlling the LEDs. The sensor noise reaches minimum values of  $1\mu\text{m}$  ( $3\sigma$ ). By implementing and tuning filters in the control scheme positioning accuracies of  $0.2\mu\text{m}$  ( $3\sigma$ ) are achieved.



Ferrofluid bearings are successfully implemented to carry the mover in all planar directions. The bearings do not limit the system in terms of precision, which is mainly determined by the sensor performance. Previous research has shown the effect of trail formation due to which the stage can decrease in height up to  $2\mu\text{m}$  per mm translation. This is something that can be accounted for by implementing height control or using the auto-focus function on digital microscopes. The ferrofluid bearings have a vertical stiffness of  $76.2\frac{\text{kN}}{\text{m}}$  and can carry loads up to 4N which is eight times the required capacity.



The actuator configuration consists of stationary coils located in between the moving magnets. When the stage rotates, the magnetic field experienced by the active coil-set weakens and changes polarity. The altering field polarity is analyzed using COMSOL simulations. Based on this model a commutation strategy is developed and successfully implemented in the control scheme to gradually activate the other coil-set, allowing the stage to smoothly rotate around its axis. The actuator coils are optimized for achieving maximum force while taking heat constraints and available power into account, resulting in a 40% higher force than required. Extensive use of the stage could cause the coils to overheat, but this can be solved by fabricating the coils on a PCB with a larger heat dissipation area.



For control purposes the stage is decoupled into three single-input-single-output (SISO) systems, thereby reducing the control complexity. A hybrid controller is proposed which uses two separately tuned PID controllers. One controller is tuned for fast and course guidance of the stage, for example during a step motion, while the other controller is activated near the desired position where high position accuracy is required. Implementing this hybrid controller can improve positioning accuracies by a factor two or more.

In conclusion: this work includes the design and analysis of a low-cost and compact planar precision stage capable of making large translations and rotate around its axis. What makes the stage unique is the innovative use of existing sensing and actuation technologies integrated in a system that is more versatile than existing solutions on the market. Also many new and interesting insights are gained which are worth further research in the future.

# 9

## Recommendations

As mentioned in the conclusion, several interesting insights are gained in the mechatronic components of this research, which are worth further investigation. An overview is provided below:

### **Recommendations regarding measuring multiple DoF using a single PSD:**

- Using corner-cubes in combination with laser diodes at the base result in a wireless stage.
- The sensing algorithm can be easily extended for measuring the system's height. In that case 4 DoF will be accounted for using only one PSD.
- The current sensor is mainly chosen for its linearity and availability in the lab, but alternative manufacturers like Hamamatsu provide cheaper sensors worth investigating. This way the component cost can be decreased even more.
- Alternative light-modulation techniques could be used in combination with battery-powered LEDs. This way it becomes possible to get rid of the wires powering the LEDs. The stage is then no longer limited in the rotational direction.

### **Recommendations considering the actuator :**

- The actuator coils are produced in-house, proving great design flexibility. In the future they can be replaced with a multilayer PCB. Not only will this result in a smaller air-gap between the magnets, but it will also improve the thermal behavior.
- The double-magnet configuration can be extended by adding another layer of magnets. This will create space for a new layer of (PCB) coils and double the actuator force and bearing stiffness.

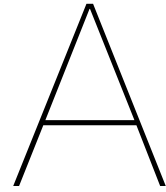
### **Recommendations considering the ferrofluid bearings:**

- The implemented magnet array containing ferrofluids has a stiffness 10 times higher than the stage built by Max Cafe, but it came with increased viscous damping. Using alternative ferrofluids (on water bases) could reduce the damping without affecting the stiffness.

### **Recommendations considering the controller:**

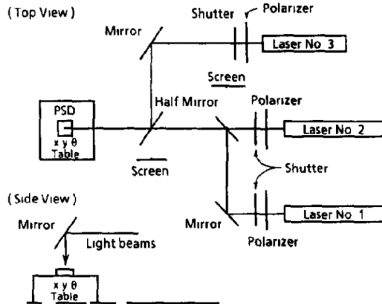
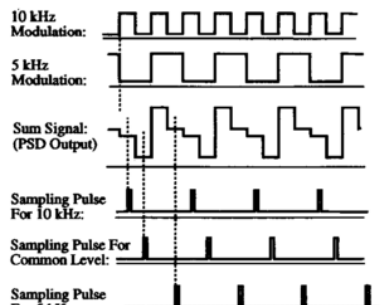
- Filtering the sensor signal resulted in lower noise values, but too much filtering is not possible because it would affect the maximum achievable control bandwidth. A hybrid controller is proposed in the control chapter. Implementing this controller could result in positioning accuracies up to  $50\text{nm}$  ( $3\sigma$ ).
- Feedforward control could potentially decrease the settling time. However, more research in the field of the varying ferrofluid damping is required. The viscous friction force changes with temperature, step size and other variables, thus a single static feedforward model could lose its predictive power and potentially worsen the step-response.



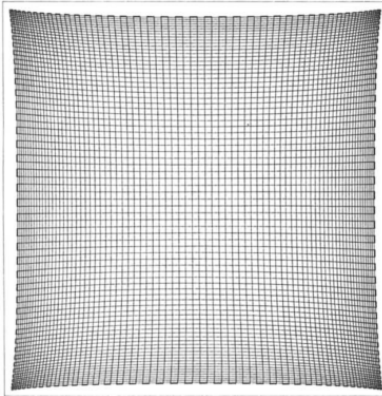


## Review of prior art

### A.1. Literature summary: Use of a PSD for position measurement and its characteristics

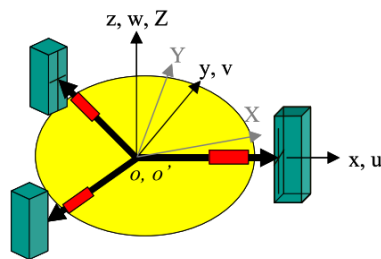
Title	Summary and takeaways
<p data-bbox="159 873 782 963"><b>On the Position Response of a Position-sensitive Detector (SD) Irradiated with Multiple Light Beams[7]</b></p> 	<p data-bbox="798 873 1409 1153">This paper describes some of key features of a PSD. The position response is measured using multiple light beams. They have experimentally proven the theory that the PSD output represents the intensity-weighted mean of the incident beam position, even when using multiple beams. Also they have proven that the position-detection non-linearity of the PSD is independent of the beam diameter.</p>
<p data-bbox="159 1292 782 1382"><b>A method for measurement of multiple light spot positions on one position-sensitive detector (PSD)[17]</b></p> 	<p data-bbox="798 1292 1409 1512">A new method for measuring the position of multiple light beams irradiating a single PSD is described. Each light source is modulated at a different frequency and then demodulated in the signal-processing circuit using a PAM scheme. The resolution, accuracy and linearity of the position measurement was not effected.</p>

### A small-distortion two-dimensional position-sensitive detector (PSD) with on-chip MOSFET switches [9]



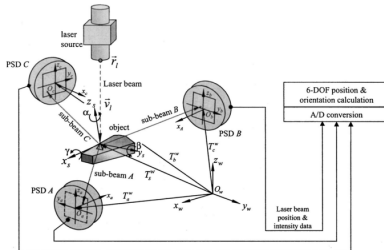
This paper is about reducing the PSD non-linearity by means of adding four wide MOSFET gates around the sensing area of a PSD. It is a good starting point for understanding the causes of sensor non-linearity, how much effect it can have on the position measurements and how to decrease the non-linearity.

### Development of a Hexapod Laser-based Metrology System for Finer Optical Beam Pointing Control [3]



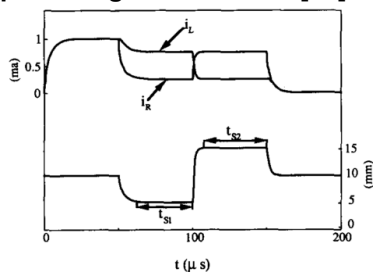
A laser metrology system, including three laser diodes and three PSDs, is used for measuring all six DoF ( $x, y, z, \theta_x, \theta_y, \theta_z$ ) of an object. Some basics, like the steps required for creating the sensor transformation matrix, can be adopted for implementing similar techniques in the measurement system of a precision stage.

### Measurement of fine 6-degrees-of-freedom displacement of rigid bodies through splitting a laser beam: experimental investigation [15]

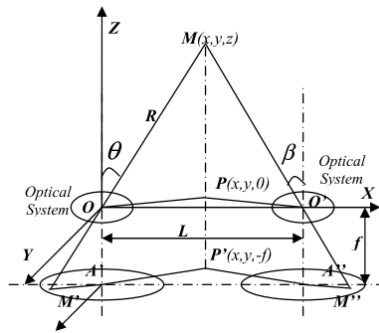


A new 6 DoF measurement system is proposed. Light from a single laser beam is projected on a three-facet mirror. The mirror is mounted on the object of interest. Depending on the position and angle of the object, light is projected in three different directions. The reflected beam is then detected by three PSD. The position and intensity signals from the sensors is used to calculate the 3-D position and orientation.

### Position dependence of the transient response of a position-sensitive detector under periodic pulsed light modulation [12]

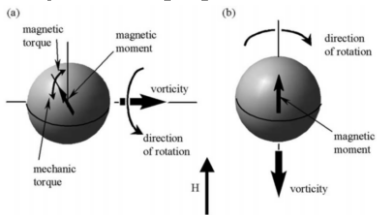
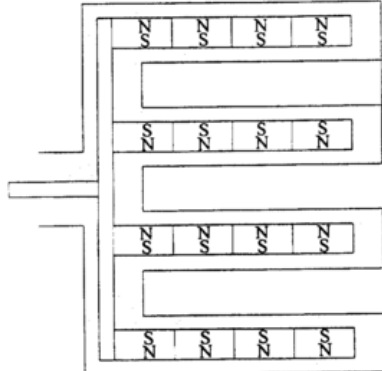
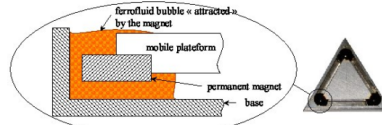
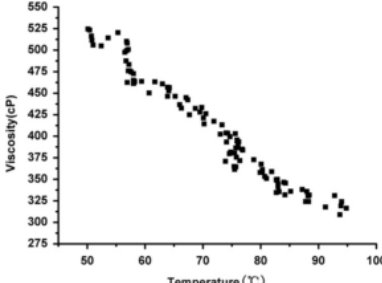


A modeled is developed for studying the output response in two cases: when only one pulse-modulated light beam is incident and when two light beams are modulated at different frequencies. The results show that the transient response consists of a position-dependent dead time and a position-independent rise time. More importantly, they showed that there is an upper limit on the usable modulation frequency.

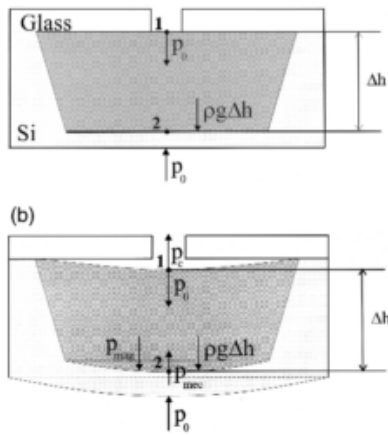
**Research of 3D spatial localizing system based on PSD [24]**

An alternative non-contact spatial localization method is described in this paper. The measurement setup consists out of two axis-parallel PSDs and lasers. By implementing their spatial localization algorithm, they achieved a resolution up to  $1\mu m$  and an error less than  $5\mu m$ .

## A.2. Literature summary: Ferrofluids and their applications

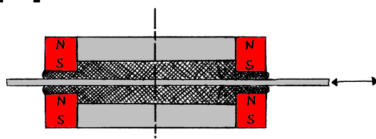
Title	Summary and takeaways
<p><b>Ferrofluids—magnetically controlled suspensions[13]</b></p> 	<p>This paper describes the possibility to control the properties and flow of ferrofluids, by using moderate magnetic fields. This paper also briefly introduces ferrofluids and their application in adaptive dampers.</p>
<p><b>Passive Magnetic Bearing Ferrofluid Stabilization With [6]</b></p> 	<p>Two NASA researchers have eventuated 22 designs analytically and some by performing measurements. The measurements including force and stiffness measurements. They have successfully demonstrated the viability of passive magnetic bearings in with ferrofluid stabilization.</p>
<p><b>Nanometer precision Six Degrees of Freedom Planar Motion Stage with Ferrofluid Bearings[2]</b></p> 	<p>In this thesis, Max Cafe has successfully implemented planar ferrofluid bearings. He has achieved nanometer precision, by reduction the friction and stick-slip bearing behavior. Also the effect of the changing ferrofluid damping coefficient was demonstrated by measuring the step response at different heights and distances.</p>
<p><b>DESIGN OF A 3 DOF DISPLACEMENT STAGE BASED ON FERROFLUIDS[8]</b></p> 	<p>The paper presents the design of a 3 DoF stage, using three ferrofluid bubbles as hydrostatic bearings. The emphasis lies on choosing appropriate volume and properties for the ferrofluid and permanent magnets.</p>
<p><b>Magnetoviscous properties of Fe<sub>3</sub>O<sub>4</sub> silicon oil based ferrofluid[15]</b></p> 	<p>The viscosity properties of ferrofluids tend to decrease with increasing temperature and increase with increasing magnetic field intensity. Also the hysteresis curve of the viscosity-field has effect on the viscosity of the FF's.</p>

**The use of ferrofluids in micromechanics [16]**



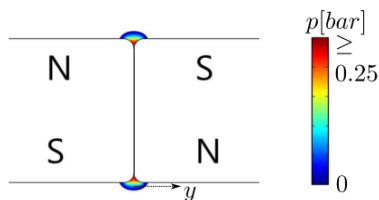
Although this paper is more about the introduction of ferrofluids in MEMS applications, the pressure calculations inside the ferrofluid are also application on macro-scale devices. Typical pressure values in the order of 40mbar are obtained.

**Ferrofluids and their applications in bearings [10]**



Alexander Mulder, a former student at the TU-Delft created this report which provides the reader an overview of ferrofluids and their application. The applications mentioned are mostly based on patents, ranging from seals to bearings. Reading this report is highly recommended for having a quick overview of ferrofluid applications.

**Planar Ferrofluid Bearings for precision stages[22]**



In this thesis the use of ferrofluids in planar bearings for precision stages is researched. By investigating the static behavior of ferrofluids, predictions can be made regarding the load capacity. A linear demonstrator stage was built to prove the applicability of ferrofluid bearings in precision stages.



# B

## Transistor network for LED modulation

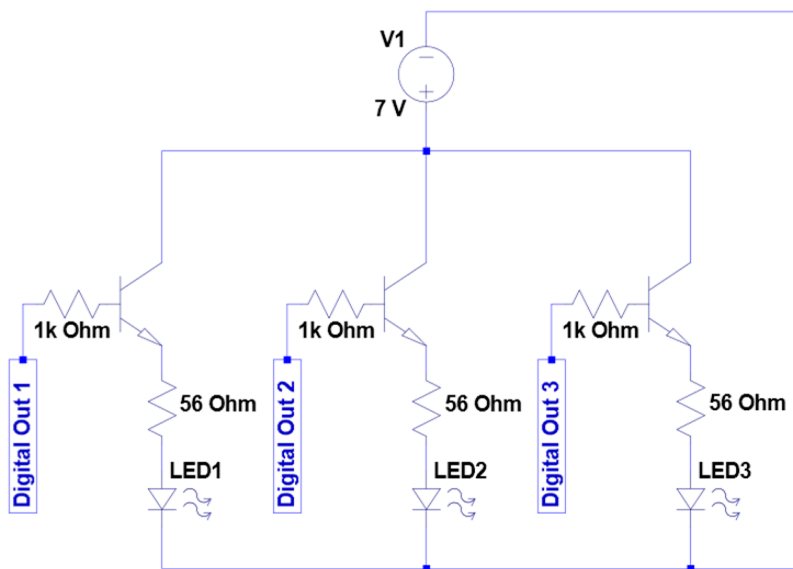
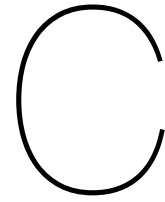


Figure B.1: Schematic overview of the transistor network schema used for LED modulation.





## Light intensity at the PSD surface

The light intensity at the surface of the PSD needs to be within certain limits. A low intensity will result in high noise levels due to the influence of stray light or other small disturbances. If the light intensity is too high, the PSD will get saturated and no reliable position signal will come out of the PSD. In Figure C.1 the position signal coming from the PSD is shown (top left). Light from an LED passes through a pinhole diameter of 0.4mm. No specific frequencies have an increased amplitude. This has mainly to do with the stable power sources used and the light shielding that prevents stray light from interfering.

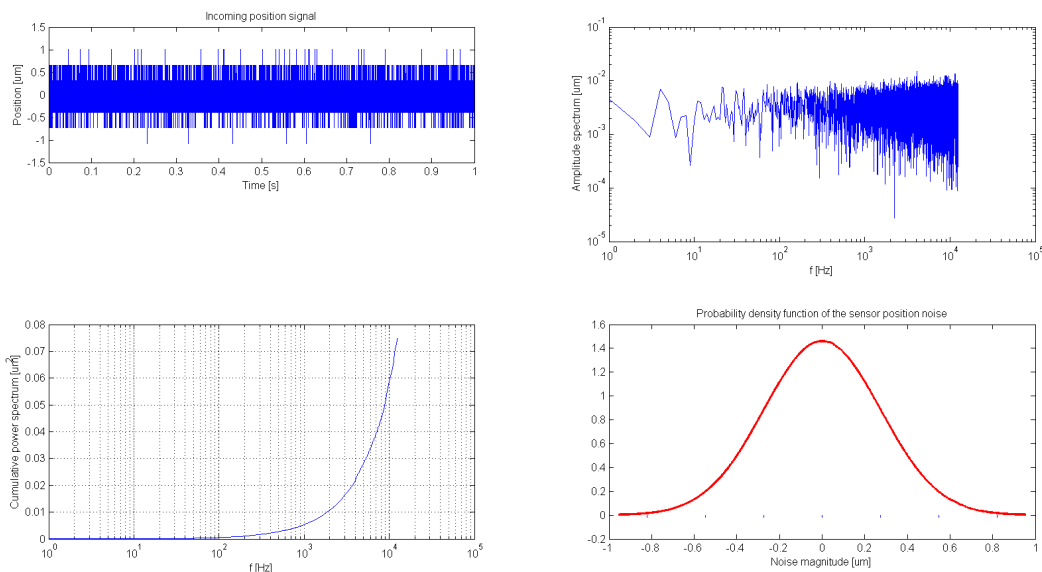
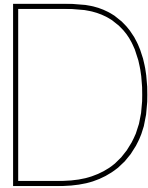


Figure C.1: PSD position signal (top left), and its amplitude spectrum, cumulative power spectrum and a Gaussian distribution of the noise





## Identification of the PSD characteristics

The PSD has a non-linear, position dependent output. In order to identify the characteristics like non-linearity, position dependent noise and maximum working area, a grid-scan measurement is performed using the 6 DoF ferrofluid stage with nanometer accuracy [2]. The input and output values are visualized in D.1. Stage starts a stepping motion starting from  $x = -5000\mu m$  and  $y = -2000\mu m$  taking steps of  $200\mu m$  with a stepping time  $0.2s$ . The PSD output is sampled at a rate of  $25kHz$  and filtered for correct use in section 4.5. Compared to the input from the interferometer, the PSD output signal contains a lot of noise. This is shown in Figure D.2.

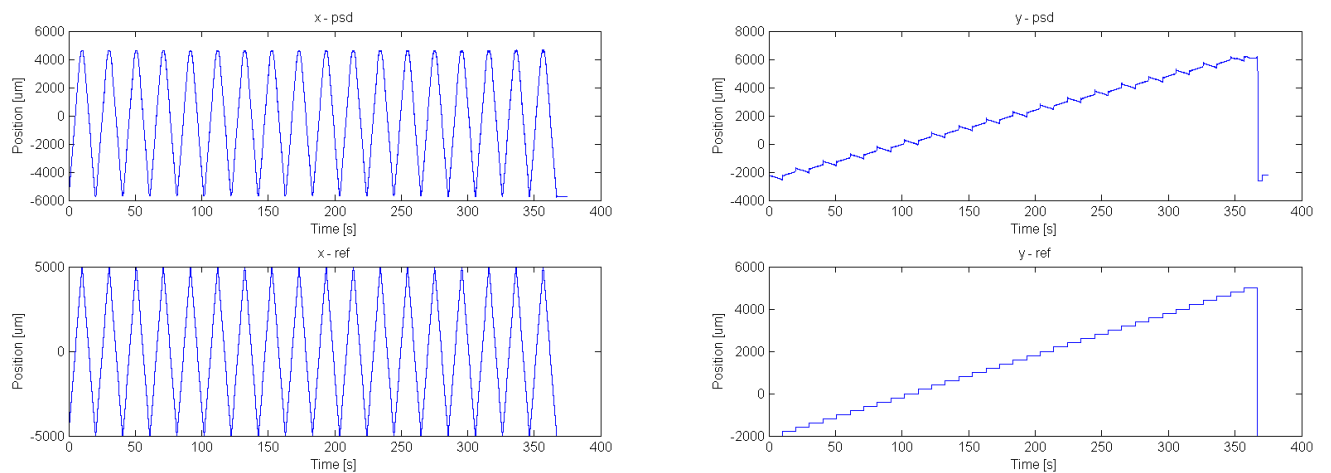


Figure D.1: Grid measurement data from the interferometer (reference value) and PSD

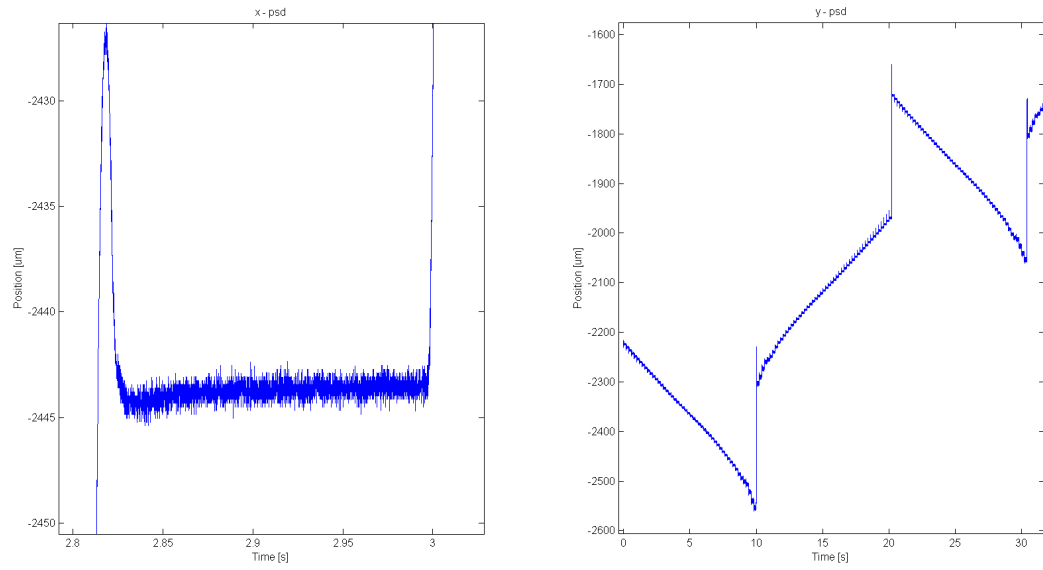
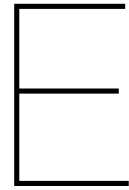


Figure D.2: Zoomed-in PSD signal value, showing the noise



## Alternative actuator concept

### 5 Coils equally distanced from each other

This concept is based on five coils, of which only three of four are active at the same time. The commutation between phase I and II takes place when coil number 4 is reaching the edge of the magnets. To compensate for this loss of power, coils 5 and 3 are activated to still be able to deliver force in the x, y and  $\theta_z$  direction. The commutation takes place five times (in order to complete a circle), before the same coil configuration is reached. Commutation has to take place after each  $8^\circ - 9^\circ$  of rotation (translations not taking into consideration yet).

The main benefit of this concept is that all coils are located at the same horizontal plane. Instead of winding coils, they can be printed on a PCB.

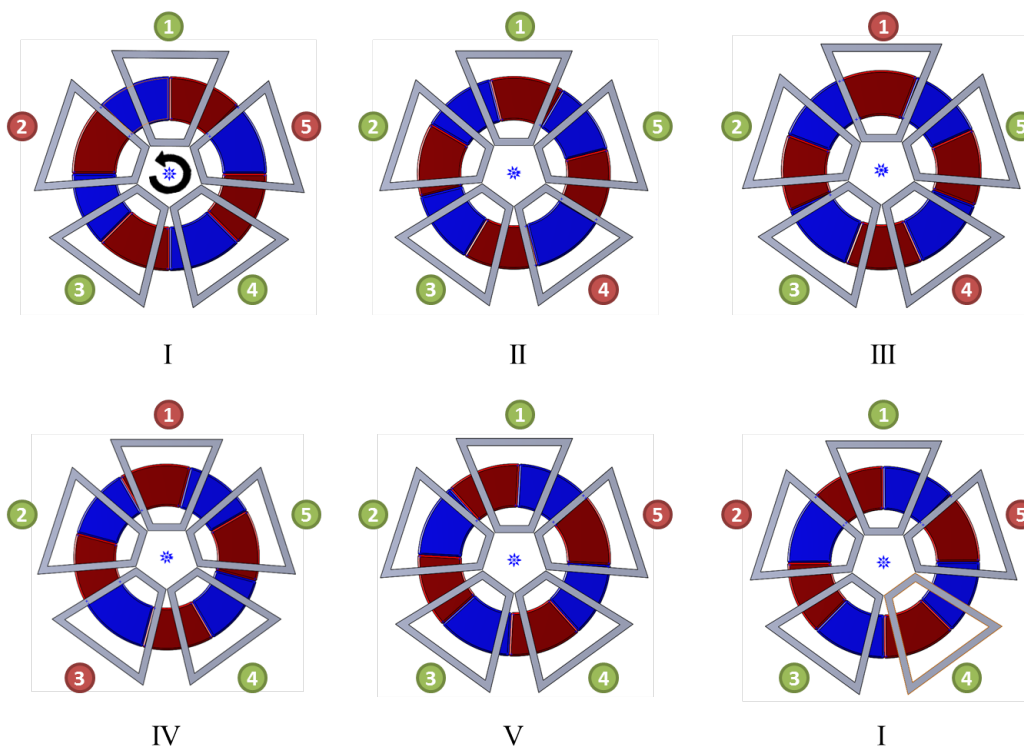


Figure E.1: 5 coils equally distanced from each other. The coils are numbered from 1-5 while the coloring indicates whether the coil is active in the position or not (green active, red not active)





## Theta controller design

In Figure F.1a the results of the system identification process in the  $\theta_z$ -direction is visualized. The model, which is equivalent to the mass-damper model created in section 6.2 but where the mass  $m$  is replaced by the moment of inertia  $I_z$ . The controller used is a PI-controller together with a first-order low-pass filter. The controller response is visualized in Figure F.1b. Multiplying the controller response with the plant response gives us the theoretical open-loop response in Figure F.1c, where the control bandwidth of 30Hz is marked together with the gain- and phase margin. Finally, the closed loop response is shown in Figure F.1d.

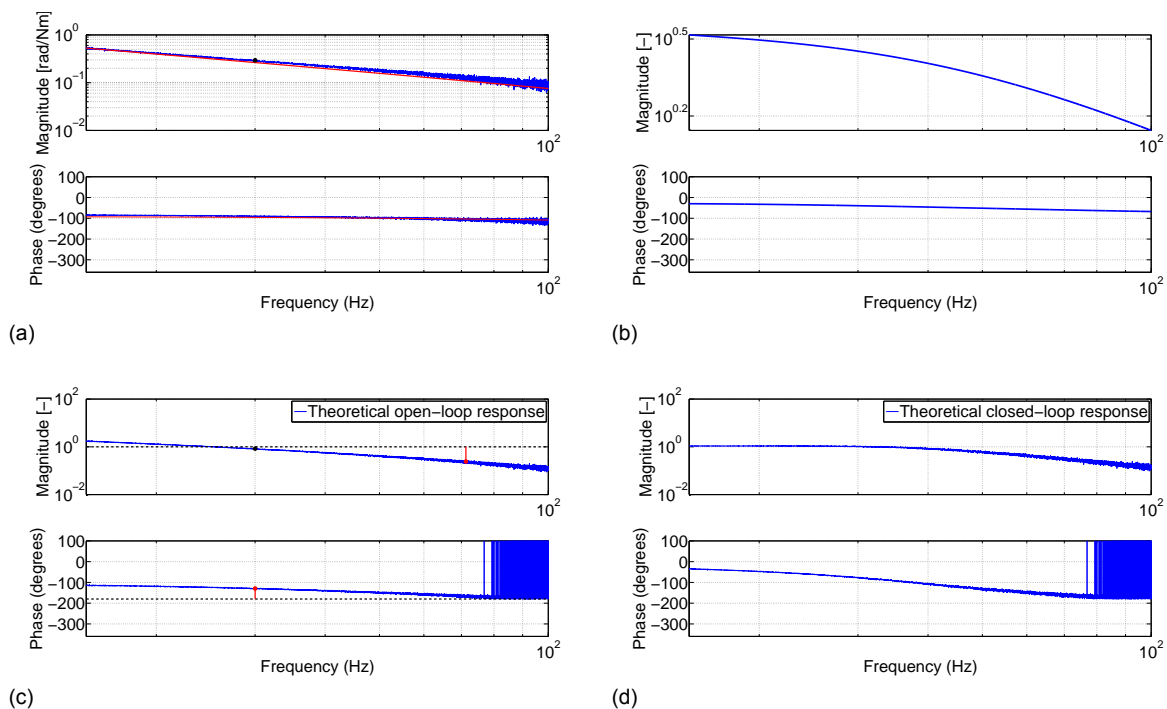


Figure F.1: (a) Frequency response of the plant  $G_{\theta_z}$ . (b) Tuned PI controller and filter response for a control bandwidth of  $f_{bw} = 30\text{Hz}$ . (c) Theoretical open loop response  $L_{\theta_z}(j\omega)$  where the phase margin ( $50^\circ$ ) and gain margin (4.1) are marked as red dots. (d) Theoretical closed loop response based in the measured plant response and modeled controller response.





## Transformation matrices

The force transformation matrices are required to convert the forces generated by the interaction between the magnets and coils relative to the center coordinate system ( $x$ ,  $y$  and  $\theta_z$ ). The relation between the force generated at each coil-set and the center coordinate system is defined in equation G.1 and G.2, where  $\mathbf{F}$  is the resultant force,  $\Phi_{F_1}$  and  $\Phi_{F_2}$  are the force transformation matrices and  $\mathbf{F}_{coils_1}$  and  $\mathbf{F}_{coils_2}$  are the forces generated by coil-set one and two.

$$\mathbf{F} = \Phi_{F_1} \mathbf{F}_{set_1} \quad (G.1)$$

$$\mathbf{F} = \Phi_{F_2} \mathbf{F}_{set_2} \quad (G.2)$$

The transformation matrices ( $\Phi_{F_1}$  and  $\Phi_{F_2}$ ) can be defined as:

$$\Phi_{F_1} = \begin{bmatrix} -\cos(22.5^\circ) & 0.5 \cdot \cos(22.5^\circ) + 0.5 \cdot \sin(22.5^\circ) & 0.5 \cdot \cos(22.5^\circ) + 0.5 \cdot \sin(22.5^\circ) \\ 0 & 0.5 \cdot \cos(22.5^\circ) + 0.5 \cdot \sin(22.5^\circ) & -0.5 \cdot \cos(22.5^\circ) - 0.5 \cdot \sin(22.5^\circ) \\ r & r & r \end{bmatrix}$$

$$\Phi_{F_2} = \begin{bmatrix} 0.5 \cdot \sin(45^\circ) & 0.5 \cdot \sin(45^\circ) & -0.5 - 0.5 \cdot \sin(45^\circ) \\ -0.5 - 0.5 \cdot \sin(45^\circ) & 0.5 + 0.5 \cdot \sin(45^\circ) & 0.5 \cdot \sin(45^\circ) \\ -r & -r & -r \end{bmatrix}$$

where  $r$  is the distance from the center of the coil to the center of the Cartesian coordinate system. One important note is that the signs (whether the values are positive or negative) inside the transformation matrix are adjusted to the actual layout of the actuators. When applying positive current, the forces relative to the moving stage act as visualized in Figure G.1. The transformation matrices are implemented in the control system exactly as depicted above.

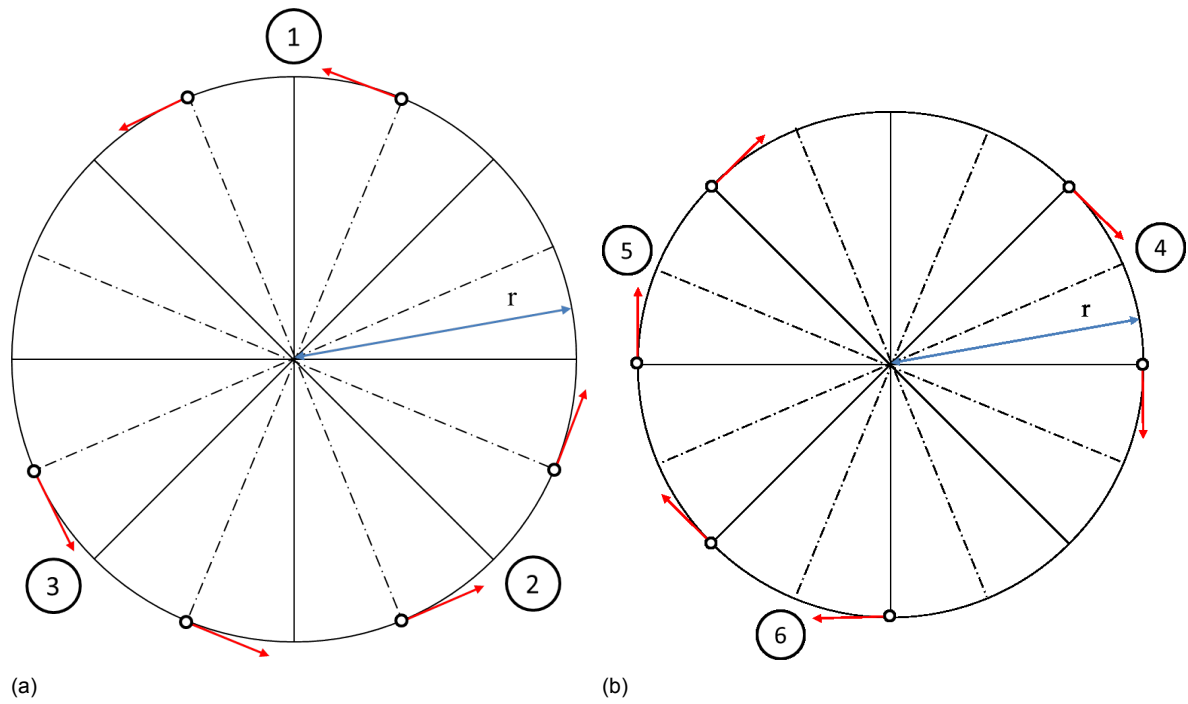


Figure G.1: (a) Position and direction of the actuator forces (coil-set 1 in (a) and for coil-set 2 in (b) with respect to the moving stage. The numbering convention of the coils refers to the transformation matrix.

The modal force matrix is defined as:

$$\mathbf{F} = [ F_x \quad F_y \quad T_z ]^T$$

and the forces generated by the coils are:

$$\mathbf{F}_{\text{set}_1} = [ F_{c_1} \quad F_{c_2} \quad F_{c_3} ]^T$$

$$\mathbf{F}_{\text{set}_2} = [ F_{c_4} \quad F_{c_5} \quad F_{c_6} ]^T$$

# Bibliography

- [1] K. Aström and R. Murray. *Feedback Systems: An Introduction for Scientists and Engineers*. Princeton University Press, Princeton, NJ, USA, 2008. ISBN 0691135762, 9780691135762.
- [2] M. Café. Nanometer precision Six Degrees of Freedom Planar Motion Stage with Ferrofluid Bearings. Master's thesis, Delft University of Technology, the Netherlands, 2014.
- [3] H. Chen, E. Hospodar, and B. Agrawal. Development of a Hexapod Laser-based Metrology System for Finer Optical Beam Pointing Control. In *22nd AIAA International Communications Satellite Systems Conference & Exhibit 2004*, number May, pages 1–8, Monterey, California, 2004.
- [4] Newport Corporation. Compact rotation stage, 360°, dc servo motor, pr series. [http://search.newport.com/?q=\\*%&x2=sku&q2=PR50CC](http://search.newport.com/?q=*%&x2=sku&q2=PR50CC). Accessed October 18, 2015.
- [5] X. He. 6-DoF stage position measurement concept for microscopy with one 2D position sensitive detector (PSD) . Master's thesis, Delft University of Technology, the Netherlands, 2014.
- [6] R. Jansen and E. DiRusso. *Passive Magnetic Bearing With Ferrofluid Stabilization*. Case Western Reserve University, 1996.
- [7] A. Kawasaki and M. Goto. On the Position Response of a Position-sensitive Detector (SD) Irradiated with Multiple Light Beams. *Sensors and Actuators A21-A23*, 23:534–537, 1990.
- [8] G. Millet and A. Hubert. Design Of A 3 Dof Displacement Stage Based On Ferrofluids. pages 656–659, 2006.
- [9] Y. Morikawa and K. Kawamura. A small-distortion two-dimensional position-sensitive detector (PSD) with on-chip MOSFET switches. *Sensors and Actuators A: Physical*, 34(2):123–129, August 1992.
- [10] A. Mulder. Ferrofluids and their applications in bearings. Technical report, Delft University of Technology, Delft, 2010.
- [11] R. Munnig Schmidt, G. Schitter, and J. van Eijk. *The Design of High Performance Mechatronics*. IOS Press BV, Amsterdam, 2011. ISBN 9781607508250.
- [12] C. Narayanan, A.B. Buckman, I. Busch-Vishniac, and W. Wang. Position dependence of the transient response of a position-sensitive detector under periodic pulsed light modulation. *IEEE Transactions on Electron Devices*, 40(9):1688–1694, 1993.
- [13] S. Odenbach. Ferrofluids-magnetically controlled suspensions. *Colloids and Surfaces A: Physicochemical and Engineering Aspects*, 217(1-3):171–178, April 2003.
- [14] S Odenbach. Recent progress in magnetic fluid research. *Journal of Physics: Condensed Matter*, 16(32):R1135–R1150, August 2004.
- [15] W. S. Park and H. Cho. Measurement of fine 6-degrees-of-freedom displacement of rigid bodies through splitting a laser beam: experimental investigation, April 2002.
- [16] R. Perez-Castillejos, J. A. Plaza, J. Esteve, P. Losantos, M. C. Acero, C. Cane, and F. Serra-Mestres. The use of ferrofluids in micromechanics. *Sensors and Actuators A: Physical*, 84(1-2): 176–180, 2000.
- [17] D. Qian, W. Wang, I. Busch-Vishniac, and A.B. Buckman. A method for measurement of multiple light spot positions on one position-sensitive detector (PSD). *IEEE TRANSACTIONS ON INSTRUMENTATION AND MEASUREMENT*, 42(1):14–18, 1993.

- [18] V. Rankov, R. J. Locke, R. J. Edens, and B. Vojnovic. An algorithm for image stitching and blending. *Proc. SPIE*, 5701(March):190–199, 2005.
- [19] W Schottky. Ueber den entstehungsort der photoelektronen in kuper-kuperoxydul- photozellen. *Physics Z.*, 31:R913–R925, November 1930.
- [20] S. Takekado. Head actuator mechanism and magnetic disk drive including the same, September 25 2001. US Patent 6,295,184.
- [21] Inc. Thorlabs. Xyz microscope stages. <https://www.thorlabs.com/newgrouppage9.cfm>. Accessed October 18, 2015.
- [22] S Van Veen. Planar Ferrofluid Bearings for precision stages. Master's thesis, Delft University of Technology, the Netherlands, 2013.
- [23] J.Torkel Wallmark. A new semiconductor photocell using lateral photoeffect. *Proceedings of the IRE*, 45(4):474–483, April 1957.
- [24] Y. Zhou, Yan G. Xie, Z. Dan, and G. Yu. Research of 3D spatial localizing system based on PSD sensor. *2009 International Conference on Measuring Technology and Mechatronics Automation, ICMTMA 2009*, 1:55–58, 2009.